UNIVERSITY OF OTTAWA

MASTER'S THESIS

---

# The role of pump amplitude on the spatial modes of bright squeezed vacuum: characterizing the evolution of the Schmidt modes

---

*Author:*
Mahtab AMOOEI

*Supervisor:*
Professor Robert W.BOYD

*A thesis submitted in fulfillment of the requirements*
*for the degree of Master of Science degree in Physics*

*in the*

Department of Physics
Faculty of Science
University of Ottawa

# Declaration of Authorship

I, Mahtab AMOOEI, declared that this thesis was all written by myself. The contributors to this thesis are:

Signed: Mahtab Amooei

Date: 24 July, 2023

# Abstract

Spontaneous parametric down-conversion (SPDC) is a nonlinear optical process in which an incident field known as the pump interacts with a nonlinear crystal to produce two output fields known as signal and idler. Due to the conservation of energy and momentum, these output fields are entangled in the temporal and spatial degrees of freedom. The gain, which represents the strength of the interaction, increases in direct proportion to the strength of the pump field. In the low-gain regime, the generated field is an entangled two-photon state. This regime continues to be routinely employed in fundamental quantum optics experiments and quantum technologies. In the high-gain regime, the generated field is a multiphoton entangled state known as a bright squeezed vacuum. The goal of this thesis is to theoretically and experimentally characterize the spatial correlations present in high-gain SPDC. In order to characterize the spatial correlations between the generated fields, we utilize the Schmidt decomposition formalism. In this study, we examine the evolution of the Schmidt modes and spectrum with increasing pump amplitude. Our work shows that the Schmidt modes expand marginally in size, and the Schmidt spectrum narrows with respect to increasing gain. The narrowing of the Schmidt spectrum, as quantified by a decrease in the Schmidt number, indicates a gradual decrease in spatial entanglement.

# Acknowledgements

First and foremost, I would like to express my deepest gratitude to my advisor, Prof. Robert Boyd. His continuous support, indispensable advice, and countless opportunities throughout my Master's degree have been invaluable. Under his guidance, I have had the privilege of working with an incredible group of people, and I would like to extend my thanks to the Boyd group as a whole for creating an exceptional laboratory and work environment.

I am immensely grateful to Dr. Girish Kulkarni for his endless patience in answering all of my questions and providing invaluable guidance throughout my projects. His mentorship and wealth of knowledge have been pivotal to the success of my research, equipping me with essential techniques and strategies that have significantly contributed to my accomplishments. I would never have been able to do this project without his expertise and valuable insights.

I would also like to express my appreciation to Dr. Jeremy Upham for his valuable advice and for consistently pushing me to improve my work. His insightful guidance and constructive feedback have been instrumental in shaping the outcome of my research.

Furthermore, I am grateful to my colleagues, Dr. Maria Chekhova, Dr. Jonathan Leach, Jeremy Rioux, Dr. Samuel Lemieux, Omid Mozafar, and Theng Loo Lim. Our fruitful discussions and exchanges of ideas have played a significant role in shaping the content of this thesis.

Lastly, I want to acknowledge the unwavering support and continuous encouragement of my parents, Maliheh and Mohammadreza, and my little brother, Aria. Their belief in me has been a constant source of motivation throughout these years of study and research.

# Contents

# List of Figures

# List of Abbreviations

| | |
|---|---|
| **SPDC** | Spontaneous Parametric Down Conversion |
| **BBO** | $\beta$-Barium Borate |
| **FWHM** | Full Width at Half Maximum |
| **SF** | Spatial Filter |
| **HWP** | Half Wave Plate |
| **PBS** | Polarizing Beam Splitter |
| **DM** | Dichroic Mirror |
| **NDF** | Neutral Density Filter |
| **BD** | Beam Dump |
| **BPF** | Band-Pass Filter |
| **EMCCD** | Electron-Multiplying Charge-Coupled Device |

# Chapter 1

# Introduction

During the early 1900s, the concepts of coherence and correlations became widely used in the field of optics. Coherence refers to the intrinsic correlations that enable physical systems to exhibit interference effects. The work of many scientists laid the foundation for these concepts. One such scientist was Michelson, who, in the 1890s, developed two interferometric techniques [1, 2, 3]. One was designed to measure energy distribution in spectral lines, and the other was developed to measure the diameters of stars, and they both relied on the concept of coherence. In 1938, Frits Zernike [4] introduced the concept of mutual intensity and degree of coherence as precise measures of spatial coherence in light fluctuations. His work marked a turning point in the development of coherence theory. It demonstrated that these quantities could be measured through simple experiments that measured the sharpness of interference fringes in Young's interference pattern.

Prior to the 1950s, the focus of scientific studies primarily revolved around field correlations. However, a significant turning point occurred during the mid-1950s when Hanbury Brown and Twiss [5, 6] conducted a series of experiments that revealed the possibility of observing correlations between intensities. These observations led to the study of higher-order correlation effects in optical fields. Subsequently, Wolf and coworkers provided a comprehensive statistical description of the optical field based on the concepts of stochastic processes [7, 8]. This description is now known as classical coherence theory. The advancements in describing the field using classical concepts have been followed by the development of a comprehensive quantum-mechanical formalism by Glauber [9, 10]. Glauber's works successfully introduced the quantum counterparts of the correlation functions featured in the classical theory.

Coherence is a common feature of both classical and quantum systems. However, there are correlations in quantum systems that have no known analog in classical systems. In particular, multiparticle quantum systems can exhibit a unique feature called quantum entanglement [11, 12, 13]. This property refers to the phenomenon where the physical state of a system composed of multiple particles cannot be decomposed into independent physical states for each individual particle. Due to their inseparability, measurements on individual particles exhibit strong correlations even when the particles are causally separated.

Einstein, Podolsky, and Rosen (EPR) investigated the essential consequences of the nonlocal correlations between entangled quantum states [11]. They proposed that for any physical theory to be valid, it must meet the requirements of local realism, which includes two conditions: locality and realism. Locality means that a measurement of one particle cannot instantaneously affect the state of another particle separated by space, while realism asserts that if a physical property of a system can be predicted with certainty without measurement, then it is an element of the reality of the particle. They demonstrated that entangled states' existence violates local realism, and therefore, they concluded that quantum theory could not provide a complete physical description of nature.

In 1964, Bell attempted to test the EPR conclusion that the quantum description of physical reality is incomplete and used it as a working hypothesis to create the local hidden variable model [14], which mathematically formalized the concept of local realism. He also formulated certain inequality relations for the measurement correlations between parts of any composite physical system, which provided a means to test the EPR assumption of local realism experimentally. Bell's inequalities demonstrated that any local realistic theory involving hidden variables would obey these inequalities, but quantum theory violated them. Numerous experiments have since been conducted to measure the correlations of entangled systems, all of which have shown a clear violation of Bell's inequalities [15, 16, 17, 18, 19, 20, 21].

The entangled states possess nonlocal correlations that can be utilized for a variety of information processing tasks, such as teleportation [22], super-dense coding [23], and efficient integer factorization [24]. These tasks are commonly considered unattainable using classical systems [25]. Consequently, studying and quantifying the correlations present in entangled quantum states is an active field of research in quantum information theory. This research has significant implications for both fundamental physics and the development of quantum technologies [26].

The most commonly employed method to generate entangled states experimentally is spontaneous parametric down-conversion (SPDC). SPDC is a second-order nonlinear optical process in which a pump photon interacts with a nonlinear medium and gets annihilated, producing a pair of photons referred to as signal and idler [27]. Due to the laws of energy, momentum, and orbital angular momentum conservation, the signal and idler photons become entangled in their temporal, spatial, and angular degrees of freedom.

In 1969, Klyshko and Zeldovich [28] conducted a theoretical study on the statistical properties of the light generated through SPDC. A year later, in 1970, Burnham and Weinberg [29] carried out experimental investigations to examine the temporal and spatial correlation between pairs of photons produced through SPDC. SPDC has been an essential process in many quantum optics experiments, such as quantum cryptography [30, 31, 32], and quantum metrology [33, 34], as well as testing foundations of quantum theory [35, 36, 37, 38].

Numerous studies have been conducted on spatial correlations in SPDC. Joobeur et al. [39] explored the general properties of spatial and temporal coherence, and Souto Ribeiro et al. [40] embarked on a series of experiments employing double-slit apertures and coincidence detection. Their initial focus was on investigating the spatial coherence properties of twin photons. Monken et al. [41] demonstrated the ability to control spatial correlations by shaping the angular spectrum of the pump beam, which opened up a wide range of applications. These applications encompassed fundamental aspects of quantum mechanics, including measuring the photonic de Broglie wavelength of a two-photon wave packet [42, 43] and observing the spatial anti-bunching of photons [44, 45]. Howell et al. [46] and D'Angelo et al. [47] formally demonstrated the entanglement between the spatial properties of twin photons.

Most research conducted on SPDC has focused on the low-gain regime [48, 49, 50, 51], which employs a low-amplitude pump. In this regime, the amplitude of each generated field is linearly dependent on the pump amplitude. In contrast, in the high-gain regime, the generated amplitudes grow exponentially with increasing pump amplitude. The low-gain regime of SPDS has received more attention both theoretically and experimentally compared to the high-gain regime due to several reasons. First, the low-gain regime is relatively easier to analyze theoretically because the photon-pair generation process can be described using perturbative approaches. Analytical derivations and modeling techniques have been developed to understand the characteristics and properties of the two-photon state produced in the low-gain regime [52, 53, 54]. Second, experimental investigations in the low-gain regime are more feasible as they require lower pump power levels, making it easier to control and manipulate the SPDC process. The high-gain regime, on the other hand, involves stronger pump intensities, which can be technically challenging to generate and handle experimentally. Additionally, perturbative approaches cannot be applied in the high-gain regime, and its theoretical characterization is more demanding. As a result, studying SPDC in the low-gain regime has been favored due to its ease of implementation both in theoretical models and experimental settings. However, SPDC is more efficient in the high gain regime and creates bright states that retain nonclassical properties, such as squeezing electric field quadratures below the shot-noise level [55]. The utilization of high-gain SPDC extends beyond the applications of its low-gain counterpart. A notable example is its utilization in generating squeezed light which can be used to enhance the sensitivity of measurements [56]. Researchers have begun exploring the high-gain regime experimentally and making efforts to explain their results.

This thesis aims to study the spatial correlations present in high-gain SPDC as a function of the pump field's strength. The approach employs the Schmidt decomposition method to determine the generated field's spatial Schmidt modes and Schmidt spectrum. Law and Eberly established the formalization of Schmidt decomposition [57], and the Schmidt modes of SPDC have been studied in the context of low gain [48, 49, 50, 51], and the high-gain regime [58, 59] for a single pump amplitude or gain. However, in this study, for the first time, we examine the evolution of the spatial Schmidt modes and Schmidt spectrum with increasing pump amplitudes. Furthermore, we investigate how the Schmidt number, which is a parameter that quantifies the degree of entanglement between the signal and idler fields, changes as the gain increases. In addition, we use the assumptions of quasi-homogeneity and rotational symmetry in our work, which greatly speeds up our computations compared to previous research [59].

The structure of this thesis is outlined as follows: In Chapter 2, we present an introduction to the fundamental concepts employed in this research, including optical coherence theory, entanglement, Schmidt decomposition, and the basics of nonlinear optics, as well as the SPDC process. In Chapter 3, we describe our theoretical characterization of the development of spatial correlations with respect to gain. In Chapter 4, we present the experimental method used to determine the Schmidt modes and spectrum for various gain values. Finally, in Chapter 5, we summarize our study and suggest some prospects for future work.

# Chapter 2

# Background

In the previous chapter, we discussed the objective of this thesis, which centers around investigating the spatial correlations exhibited by high-gain SPDC. To achieve this objective, it is crucial to establish a solid understanding of fundamental concepts. In this chapter, we introduce the essential concepts required for our investigation. Within this chapter, we will introduce the classical coherence theory established by Wolf, as well as its quantum counterpart developed by Glauber. Furthermore, we will explore quantum entanglement and SPDC and Schmidt decomposition. By the end of this chapter, we will possess a comprehensive understanding of the key concepts essential to our research, enabling us to engage in a comprehensive analysis of the spatial correlations associated with SPDC.

## 2.1 Introduction to optical coherence

Coherence refers to the correlation between waves that are either temporally or spatially separated. When knowledge of the wave function of light at one point in space and time allows for a precise prediction of the wave function at another point in space and time, the waves are considered coherent [60]. For instance, the output of a laser is typically a good example of coherent waves. In contrast, most sources of illumination are either partially coherent or incoherent, meaning that their waves do not exhibit a significant correlation. The concept of optical coherence was first introduced in optics in connection with interference and the detection of optical fields [4, 61, 8]. Coherence quantifies the wave nature of light, i.e., the ability to exhibit interference effects. Interference effects that arise from the superposition of two light beams originating from the same source are the most straightforward manifestation of coherence in optical fields [62]. The famous Young double-slit experiment demonstrates how coherent light creates a distinct intensity pattern on a screen as it passes through two slits and interferes. As lasers and other innovative light sources emerged, optical coherence phenomena were systematically classified, including coherence effects of various orders and a full statistical portrayal of optical fields. This field of study is known as optical coherence theory, which has been formulated using both classical and quantum theoretical frameworks [8, 63].

The statistical portrayal of fluctuations linked with all electromagnetic fields is an essential aspect of coherence theory. Therefore, when it comes to analyzing light's coherence and polarization properties, a deterministic model of optical fields is inadequate. Instead, a systematic description of light's statistical properties necessitates assuming that the complex electric field vector $\boldsymbol{E}(\boldsymbol{r};t)$ is random in nature. Decomposing the field into a Fourier integral allows us to conveniently describe the electric field using a complex signal, With the observed, real part of the field being [63, 64, 7],

$$\begin{aligned}\boldsymbol{E}(\boldsymbol{r};t) = \int_{-\infty}^{\infty} \tilde{\boldsymbol{E}}(\boldsymbol{r};\omega)e^{-i\omega t}d\omega = \int_{0}^{\infty} \tilde{\boldsymbol{E}}(\boldsymbol{r};\omega)e^{-i\omega t}d\omega + \int_{-\infty}^{0} \tilde{\boldsymbol{E}}(\boldsymbol{r};\omega)e^{-i\omega t}d\omega \\ = \boldsymbol{E}^{+}(\boldsymbol{r};t) + \boldsymbol{E}^{-}(\boldsymbol{r};t) = 2Re\{\boldsymbol{E}^{+}(\boldsymbol{r};t)\}.\end{aligned} \tag{2.1}$$

Since $\boldsymbol{E}(\boldsymbol{r};t)$ is real, the complex amplitude $\tilde{\boldsymbol{E}}(\boldsymbol{r};\omega)$ follows the symmetry property of $\tilde{\boldsymbol{E}}(\boldsymbol{r};\omega)^* = \tilde{\boldsymbol{E}}(\boldsymbol{r};-\omega)$ [64], where $\omega$ denotes frequency and $\boldsymbol{E}^{-}(\boldsymbol{r};t)$ and $\boldsymbol{E}^{+}(\boldsymbol{r};t)$ are negative-frequency and positive-frequency fields respectively, and they are complex conjugate of each other, meaning $\boldsymbol{E}^{+}(\boldsymbol{r};t) = (\boldsymbol{E}^{-}(\boldsymbol{r};t))^*$. The positive-frequency field, $\boldsymbol{E}^{+}(\boldsymbol{r};t)$ is called **the complex analytic signal** associated with the real electric field vector.

As we mentioned before, the nature of $\boldsymbol{E}^{+}(\boldsymbol{r};t)$ is stochastic. Therefore, each of its components can be represented by statistical ensembles $\{\boldsymbol{E}_i^{+}(\boldsymbol{r};t)\}$, where i = x, y, z represents three arbitrary mutually orthogonal directions in space. The first-order coherence function captures light's most fundamental or basic correlation properties in the space-time domain at their simplest or lowest order. In line with Glauber's convention, this function is called the first-order coherence function and is denoted as $G^{(1)}(\boldsymbol{r_1},\boldsymbol{r_2};t_1,t_2)$ (as opposed to Mandel Wolf's numbering convention where it would be considered the second-order coherence function). Its elements are determined as [60]

$$G_{ij}^{(1)}(\boldsymbol{r_1},\boldsymbol{r_2};t_1,t_2) \equiv \langle E_i^{-}(\boldsymbol{r_1};t_1)E_j^{+}(\boldsymbol{r_2};t_2)\rangle. \tag{2.2}$$

Assuming that the stochastic process is statistically stationary, the components of $G_{ij}^{(1)}(\boldsymbol{r_1},\boldsymbol{r_2};t_1,t_2)$ depend only on the time difference $\tau = t_2 - t_1$ [7]

$$G^{(1)}(\boldsymbol{r_1},\boldsymbol{r_2};t_1,t_2) = G^{(1)}(\boldsymbol{r_1},\boldsymbol{r_2};\tau) = \langle E^{-}(\boldsymbol{r_1};t)E^{+}(\boldsymbol{r_2};t+\tau)\rangle. \tag{2.3}$$

The average intensity at location $\boldsymbol{r}$ is given by

$$I(\boldsymbol{r},t) = \langle|\boldsymbol{E}^{(+)}(\boldsymbol{r};t)|^2\rangle = G^{(1)}(\boldsymbol{r},\boldsymbol{r};0). \tag{2.4}$$

Similarly, higher-order coherence functions can be defined as:

$$G^{(k)}(\boldsymbol{r_1},\boldsymbol{r_2},...,\boldsymbol{r_k};t_1,t_2,...,t_k) = \langle E^-(\boldsymbol{r_1};t_1)E^-(\boldsymbol{r_2};t_2)...E^-(\boldsymbol{r_k};t_k)E^+(\boldsymbol{r_1};t_1)E^+(\boldsymbol{r_2};t_2)...E^+(\boldsymbol{r_k};t_k)\rangle, \quad (2.5)$$

where $k$ indicates the order of coherence function. First and second-order coherence functions will be discussed in detail in the following sections.

## 2.2 First-order spatial coherence

Let us focus on the concept of **spatial coherence**, which refers to the correlation in phase between different points of the radiation field that are spatially separated. In order to determine the coherence of fields at two distinct spatial points, it is necessary to interfere the fields. The visibility of fringes generated in Young's interference experiment is the simplest illustration of the coherence characteristics of light [62, 60, 7, 65].

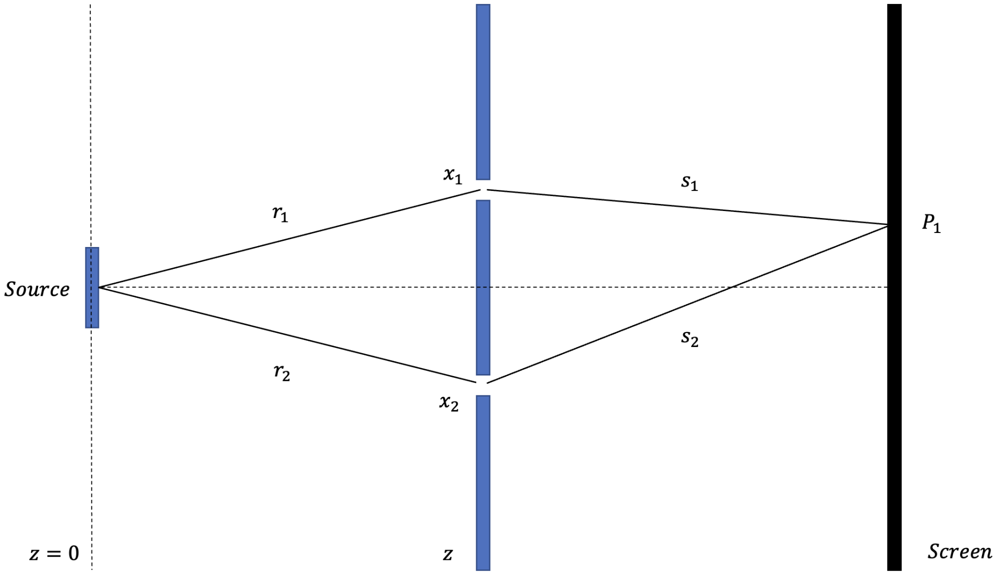

FIGURE 2.1: Schematic representation of spatial interference in Young's double-slit interferometer. The two slits are located at $r_1$ and $r_2$, and their distances from the detection point P(r) are denoted by $s_1$ and $s_2$, respectively.

Fig 2.1 illustrates a basic configuration for studying spatial interference utilizing Young's double-slit arrangement. A quasi-monochromatic source is located at z = 0. Quasi-monochromatic beam refers to a field whose effective frequency bandwidth $\Delta\omega_0$

is small compared to its mean frequency $\omega_0$ [7]. The double-slit plane receives the light at position z. Photons from the source can take two potential pathways to reach the observation screen: alternative 1 involves passing through the upper slit at position $\boldsymbol{r}_1$, while alternative 2 involves passing through the lower slit at position $\boldsymbol{r}_2$. As long as the fields in the two alternatives remain coherent with each other, the interference occurs when the probability amplitudes of a photon in the two alternatives are combined with the difference in path lengths to the two slits given by $\Delta\boldsymbol{r} = \boldsymbol{r}_1 - \boldsymbol{r}_2$.

The field at some point P(r) on the screen is formed by the combination of the fields propagating from the upper slit and the lower slit:

$$\boldsymbol{E}^{(+)}(\boldsymbol{r};t) = k_1\boldsymbol{E}^{(+)}(\boldsymbol{r_1};t-t_1) + k_2\boldsymbol{E}^{(+)}(\boldsymbol{r_2};t-t_2), \tag{2.6}$$

where $k_1$ and $k_2$ are two imaginary constants that depend on the dimensions of the apertures and the geometry of the setup and $t_1 = \frac{s_1}{c}$, and $t_2 = \frac{s_2}{c}$. We calculate the instantaneous intensity at point $P(r)$ using (2.4)

$$I(\boldsymbol{r},t) = |k_1|^2 I(\boldsymbol{r_1},t_1) + |k_2|^2 I(\boldsymbol{r_2},t_1) + 2\mathrm{Re}\{k_1^* k_2 \boldsymbol{E}^{(-)}(\boldsymbol{r_1};t-t_1)\boldsymbol{E}^{(+)}(\boldsymbol{r_2};t-t_2)\}. \tag{2.7}$$

Consequently, The ensemble average intensity at point P(r) is:

$$\langle I(\boldsymbol{r},t)\rangle = |k_1|^2\langle I(\boldsymbol{r_1},t_1)\rangle + |k_2|^2\langle I(\boldsymbol{r_2},t_2)\rangle + 2\mathrm{Re}\{k_1^* k_2 G^{(1)}(\boldsymbol{r_1},\boldsymbol{r_2};\tau)\}, \tag{2.8}$$

where $\tau = t_2 - t_1 = (s_2 - s_1)/c$ and

$$G^{(1)}(\boldsymbol{r_1},\boldsymbol{r_2};\tau) = \langle E^{-}(\boldsymbol{r_1};t)E^{+}(\boldsymbol{r_2};t+\tau)\rangle. \tag{2.9}$$

The first two terms in (2.8) represent the contributions of each of the slits to the total intensity in the absence of the other. The fringes appear due to the term that contains the mutual coherence function $G^{(1)}(\boldsymbol{r_1},\boldsymbol{r_2};\tau)$. One can normalize the first-order coherence function as

$$g^{(1)}(\boldsymbol{r_1},\boldsymbol{r_2};\tau) = \frac{G^{(1)}(\boldsymbol{r_1},\boldsymbol{r_2};\tau)}{\sqrt{G^{(1)}(\boldsymbol{r_1},\boldsymbol{r_1};0)G^{(1)}(\boldsymbol{r_2},\boldsymbol{r_2};0)}} = \frac{G^{(1)}(\boldsymbol{r_1},\boldsymbol{r_2};\tau)}{\sqrt{I(\boldsymbol{r_1},t)I(\boldsymbol{r_2},t)}}, \tag{2.10}$$

where $g^{(1)}(\boldsymbol{r_1},\boldsymbol{r_2};\tau)$ is known as the **first-order degree of coherence**. Using the Cauchy-Schwartz inequality, one can prove that

$$0 \leq |g^{(1)}(\boldsymbol{r_1},\boldsymbol{r_2};\tau)| \leq 1. \tag{2.11}$$

As the mutual coherence function $G^{(1)}(\boldsymbol{r_1},\boldsymbol{r_2};\tau)$ is in general complex, then one can write [7]

$$g^{(1)}(\boldsymbol{r_1},\boldsymbol{r_2};\tau) = |g^{(1)}(\boldsymbol{r_1},\boldsymbol{r_2};\tau)|e^{i\phi(\boldsymbol{r_1},\boldsymbol{r_2};\tau)}, \tag{2.12}$$

where $\phi(\boldsymbol{r_1},\boldsymbol{r_2};\tau) = \arg\{g^{(1)}(\boldsymbol{r_1},\boldsymbol{r_2};\tau)\}$. Using the above equation, the average intensity (2.8) is written as:

$$\begin{aligned}\langle I(\boldsymbol{r},t)\rangle &= |k_1|^2\langle I(\boldsymbol{r_1},t_1)\rangle + |k_2|^2\langle I(\boldsymbol{r_2},t_2)\rangle \\ &+ 2|k_1||k_2|\sqrt{I(\boldsymbol{r_1},t_1)I(\boldsymbol{r_2},t_2)}|g^{(1)}(\boldsymbol{r_1},\boldsymbol{r_2};\tau)|\cos\left(\phi(\boldsymbol{r_1},\boldsymbol{r_2};\tau)\right).\end{aligned} \tag{2.13}$$

As mentioned before, the visibility of fringes is a measure of coherence. The visibility of the fringes at point $P(r)$ is defined as

$$V(\boldsymbol{r}) = \frac{I_{max} - I_{min}}{I_{max} + I_{min}}. \tag{2.14}$$

Using (2.13) we obtain

$$V(\boldsymbol{r}) = \frac{2|k_1||k_2|\sqrt{I(\boldsymbol{r_1},t_1)I(\boldsymbol{r_2},t_2)}}{|k_1|^2\langle I(\boldsymbol{r_1},t_1)\rangle + |k_2|^2\langle I(\boldsymbol{r_2},t_2)\rangle}|g^{(1)}(\boldsymbol{r_1},\boldsymbol{r_2};\tau)|. \tag{2.15}$$

We note that there is a direct proportion between the visibility of the fringes and the degree of coherence of the superposing fields. If the two fields have equal intensity, the visibility will have the form

$$V(\boldsymbol{r}) = |g^{(1)}(\boldsymbol{r_1},\boldsymbol{r_2};\tau)|. \tag{2.16}$$

When $g^{(1)}(\boldsymbol{r_1},\boldsymbol{r_2};\tau) = 1$, the fringes exhibit maximum contrast, and the light is considered to be fully spatially coherent. On the contrary, when $g^{(1)}(\boldsymbol{r_1},\boldsymbol{r_2};\tau) = 0$, no interference is observed, and the light is characterized as spatially incoherent. When the magnitude of $g^{(1)}(\boldsymbol{r_1},\boldsymbol{r_2};\tau)$ falls between 0 and 1, the light is considered to be partially coherent. Figure 2.2 depicts the first-order degree of coherence for fully coherent light and thermal light. The nature of thermal light will be discussed in detail in section 2.5.

## 2.3 Coherent mode decomposition of the first-order spatial coherence function

Mercer's theorem states that any continuous function that is Hermitian and non-negative definite can be expressed in the form of Mercer's expansion [63, 66, 67, 68]. Since the first-order spatial correlation function satisfies the above conditions, one can write:

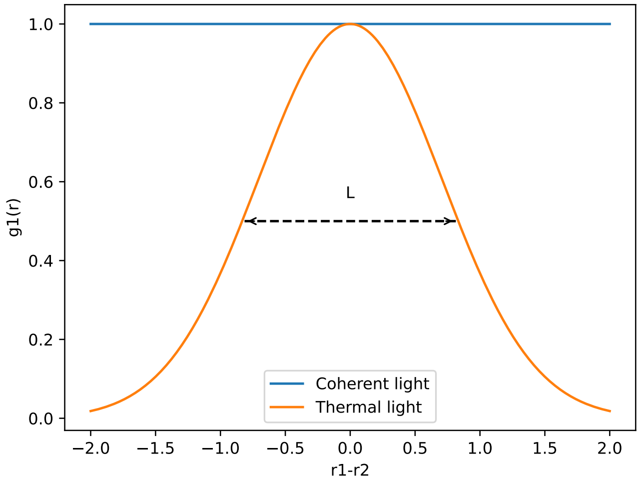

FIGURE 2.2: First-order degree of coherence function $g^{(1)}(\boldsymbol{r})$ for fully coherent light (blue line) and thermal light(orange line) as a function of $\boldsymbol{r} = \boldsymbol{r}_1 - \boldsymbol{r}_2$. The dashed line represents the spatial coherence length L which is the FWHM of $g^{(1)}(\boldsymbol{r})$ for thermal light.

$$G^{(1)}(\boldsymbol{r_1}, \boldsymbol{r_2}) = G^{(1)}(\boldsymbol{r_1}, \boldsymbol{r_2}; 0) = \sum_n \lambda_n u_n^*(\boldsymbol{r_1}) u_n(\boldsymbol{r_2}), \tag{2.17}$$

where $\lambda_n$ are the eigenvalues and $u_n(\boldsymbol{r})$ are the eigenfunctions of the homogeneous Fredholm integral equation of the second kind [69],

$$\int G^{(1)}(\boldsymbol{r_1}, \boldsymbol{r_2}) u_n(\boldsymbol{r_1}) d\boldsymbol{r_1} = \lambda_n u_n(\boldsymbol{r_2}). \tag{2.18}$$

The first-order coherence function possesses Hermitian symmetry, i.e.,

$$G^{(1)^*}(\boldsymbol{r_2}, \boldsymbol{r_1}) = G^{(1)}(\boldsymbol{r_1}, \boldsymbol{r_2}). \tag{2.19}$$

And it is a non-negative definite function, i.e.,

$$\int\int G^{(1)}(\boldsymbol{r_1}, \boldsymbol{r_2}) f^*(\boldsymbol{r_1}) f(\boldsymbol{r_2}) d\boldsymbol{r_1} d\boldsymbol{r_2} \geq 0, \tag{2.20}$$

where $f(\boldsymbol{r})$ is any square-integrable function [66]. The first-order coherence function's Hermiticity and non-negative definiteness ensure that its eigenvalues are both non-negative and real, i.e., $\lambda_n \geq 0$.

When it comes to eigenfunctions and their corresponding eigenvalues, it is important to note that any two eigenfunctions associated with different eigenvalues are always orthogonal to each other, and if we normalize the eigenfunctions, they satisfy the orthonormality condition

$$\int_{-\infty}^{\infty} u_n^*(\boldsymbol{r}) u_m(\boldsymbol{r}) d\boldsymbol{r} = \delta_{nm}, \tag{2.21}$$

where $\delta_{nm}$ is the Kronecker symbol. However, in cases where there is a degeneracy, and more than one eigenfunction belongs to the same eigenvalue, the eigenfunctions may not be mutually orthogonal. In such cases, the Gram-Schmidt procedure [70] can be used to orthogonalize the eigenfunctions. This procedure allows us to form an orthonormal set of eigenfunctions for integral Equation (2.18).

Equation (2.17) is known as **coherent mode representation** of the first-order spatial coherence function. In order to clarify the meaning of coherent modes, we start by writing the equation (2.17) as [66, 67]

$$G^{(1)}(\boldsymbol{r_1}, \boldsymbol{r_2}) = \sum_n \lambda_n G_n^{(1)}(\boldsymbol{r_1}, \boldsymbol{r_2}), \tag{2.22}$$

where

$$G_n^{(1)}(\boldsymbol{r_1}, \boldsymbol{r_2}) = u_n^*(\boldsymbol{r_1}) u_n(\boldsymbol{r_2}). \tag{2.23}$$

Now we write the first-order degree of coherence (2.10) for $G_n^{(1)}(\boldsymbol{r_1}, \boldsymbol{r_2}; 0)$ as

$$g_n^{(1)}(\boldsymbol{r_1}, \boldsymbol{r_2}) = \frac{G_n^{(1)}(\boldsymbol{r_1}, \boldsymbol{r_2})}{\sqrt{G_n^{(1)}(\boldsymbol{r_1}, \boldsymbol{r_1}) G_n^{(1)}(\boldsymbol{r_2}, \boldsymbol{r_2})}}. \tag{2.24}$$

According to (2.23), the above relation can be written as

$$g_n^{(1)}(\boldsymbol{r_1}, \boldsymbol{r_2}) = \frac{u_n^*(\boldsymbol{r_1}) u_n(\boldsymbol{r_2})}{|u_n(\boldsymbol{r_1})||u_n(\boldsymbol{r_2})|}, \tag{2.25}$$

and therefore

$$|g_n^{(1)}(\boldsymbol{r_1}, \boldsymbol{r_2})| = 1. \tag{2.26}$$

The coherent-mode representation of the field, as given by expansion (2.17), implies that each mode in the field corresponds to a spatially fully coherent component. In other words, the first-order coherence function of the field can be expressed as an incoherent sum of contributions from modes that are entirely coherent in the spatial domains.

## 2.4 Second-order spatial coherence

We now shift the discussion to the second-order correlation function. One well-known experiment that probes the higher-order coherence properties of a field is the Hanbury Brown-Twiss experiment [71], which is depicted in Figure 2.3. Here, a light beam is split into two beams and detected by detectors $D_1$ and $D_2$ located at positions $r_1$ and $r_2$ from the beam splitter, respectively. The beams are then multiplied and averaged in a correlator. Unlike the double-slit experiment, the detection of higher-order interference effects in this experiment relies on measuring two intensities at different positions rather than the correlation between two fields [65].

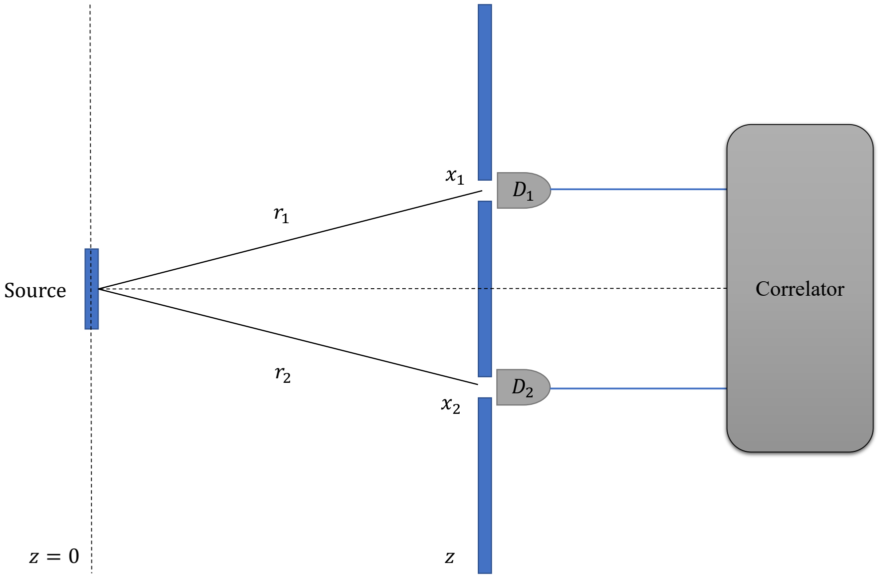

FIGURE 2.3: Schematic representation of Hanbury Brown-Twiss interferometer. The interferometer is similar to Young's double slit interferometer, except that two detectors are placed behind the slits for joint-detection of the intensities at locations $\boldsymbol{r}_1$ and $\boldsymbol{r}_2$, and a correlator is used to multiply and average the resulting product.

The intensity correlation function, namely the second-order coherence function, has the form

$$G^{(2)}(\boldsymbol{r_1}, \boldsymbol{r_2}; \tau) = \langle I(\boldsymbol{r_1}; t) I(\boldsymbol{r_2}; t+\tau)\rangle = \langle E^{-}(\boldsymbol{r_1}; t) E^{-}(\boldsymbol{r_2}; t+\tau) E^{+}(\boldsymbol{r_1}; t) E^{+}(\boldsymbol{r_2}; t+\tau)\rangle. \tag{2.27}$$

As demonstrated, the second-order correlation function displays a fourfold correlation of the amplitude $E(\boldsymbol{r};t)$. When the intensity correlation function is normalized, it becomes possible to express the second-order degree of coherence as

$$g^{(2)}(\boldsymbol{r_1},\boldsymbol{r_2};\tau)=\frac{G^{(2)}(\boldsymbol{r_1},\boldsymbol{r_2};\tau)}{\langle I(\boldsymbol{r_1};t)\rangle\langle I(\boldsymbol{r_2};t+\tau)\rangle}. \tag{2.28}$$

Second-order coherence is attained when the two condition $g^{(2)}(\boldsymbol{r_1},\boldsymbol{r_2};\tau)=1$ and $g^{(1)}(\boldsymbol{r_1},\boldsymbol{r_2};\tau)=1$ hold simultaneously, whereas if $g^{(2)}(\boldsymbol{r_1},\boldsymbol{r_2};\tau)>1$, the field is considered less coherent. When $g^{(2)}(\boldsymbol{r_1},\boldsymbol{r_2};\tau)=1$, the second-order degree of coherence is factorizable [72], i.e.

$$G^{(2)}(\boldsymbol{r_1},\boldsymbol{r_2};\tau)=\langle I(\boldsymbol{r_1};t)\rangle\langle I(\boldsymbol{r_2};t+\tau)\rangle. \tag{2.29}$$

Factorizable $G^{(2)}(\boldsymbol{r_1},\boldsymbol{r_2};\tau)$ indicates that there is no correlation between the two intensities $I(\boldsymbol{r_1};t)$ and $I(\boldsymbol{r_2};t+\tau)$. It is not possible to set an upper limit for the second-order correlation function. However, the intensities are always positive, so we have

$$0\leq g^{(2)}(\boldsymbol{r_1},\boldsymbol{r_2};\tau)<\infty. \tag{2.30}$$

For the special case of a single field where, $\boldsymbol{r_1}=\boldsymbol{r_2}$ and $\tau=0$,

$$g^{(2)}(\boldsymbol{r_1},\boldsymbol{r_2};\tau)\leq g^{(2)}(\boldsymbol{r_1},\boldsymbol{r_1};0), \tag{2.31}$$

which implies that the value of the second-order coherence function can never exceed its value for zero time delay of a single field.

For a thermal light that has a spectral line with a Gaussian lineshape, $g^{(2)}(\boldsymbol{r_1},\boldsymbol{r_2};0)$ is given by

$$g^{(2)}(\boldsymbol{r_1},\boldsymbol{r_2};0)=1+\exp\left[-\pi(\frac{\boldsymbol{r_1}-\boldsymbol{r_2}}{L})^2\right], \tag{2.32}$$

where $L$ denotes the coherent length. When $\boldsymbol{r_1}$ and $\boldsymbol{r_2}$ are equal, the value of $g^{(2)}(\boldsymbol{r_1},\boldsymbol{r_2};0)$ is 2, but as the distance between the two points increases and becomes much larger than the coherence length, the value of $g^{(2)}(\boldsymbol{r_1},\boldsymbol{r_2};0)$ decreases to 1. Figure 2.4 depicts the second-order degree of coherence for fully coherent light and thermal light.

## 2.5 Relationship between first-order and second-order spatial coherence for thermal fields

Chaotic radiation refers to electromagnetic radiation that exhibits irregular and unpredictable fluctuations in its intensity and phase. This type of radiation is generated by a wide range of sources, including thermal sources such as blackbodies. Unlike coherent

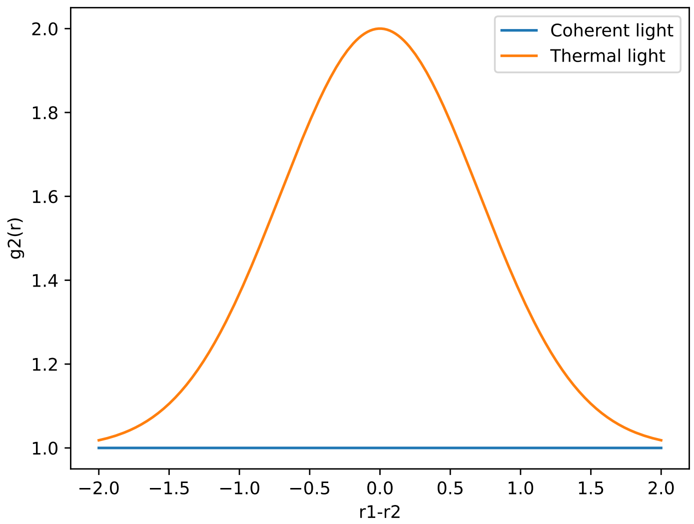

FIGURE 2.4: Second-order degree of coherence function $g^{(1)}(\boldsymbol{r})$ for fully coherent light (blue line) and thermal light(orange line) as a function of $\boldsymbol{r} = \boldsymbol{r}_1 - \boldsymbol{r}_2$.

sources, which radiate light with a well-defined phase relationship between its waves, in the case of a chaotic-thermal source, the atoms emit radiation in an uncorrelated manner, meaning that the phases of the emitted waves are independent of each other. However, the statistical properties of chaotic radiation can still be analyzed using correlation functions.

The coherence properties of chaotic-thermal light differ from those of coherent radiation due to the lack of phase correlation between the emitted waves. This results in a second-order coherence function that cannot be expressed as the product of two intensities (in contrast with equation (2.29)). Consequently, the measured intensities become dependent on each other, meaning that fluctuations in one intensity correlate with fluctuations in the other. The existence of nontrivial second-order coherence, or correlation of thermal radiation, was discovered through experiments by Hanbury Brown and Twiss in 1956. This discovery provided significant insights into the nature of chaotic-thermal radiation and has played a crucial role in developing modern-day optics and photonics [72]. One of the key insights provided by the experiment is that the non-factorizable second-order correlation function of thermal light can be expressed in terms of its first-order coherence function. This important characteristic of thermal light will be discussed in detail in this section [73].

Let us imagine a radiation source that is comprised of numerous independent point sub-sources. Therefore, the overall electric field at any given point and time is the summation of the fields produced by individual sub-sources, i.e.

$$E(\boldsymbol{r};t) = \sum_i E_i(\boldsymbol{r};t). \tag{2.33}$$

As a result, The radiation fields at two different positions, namely $E(\boldsymbol{r_1};t)$ and $E(\boldsymbol{r_1};t+\tau)$, arise due to the combination or superposition of sub-fields excited by each of the independent sub-sources.

Assuming that a chaotic light source consists of N un-correlated radiating atoms. One can write the second-order coherence function (2.27) as:

$$\begin{aligned} G^{(2)}(\boldsymbol{r_1},\boldsymbol{r_2};\tau) &= \langle E^-(\boldsymbol{r_1};t)E^+(\boldsymbol{r_1};t)E^-(\boldsymbol{r_2};t+\tau)E^+(\boldsymbol{r_2};t+\tau)\rangle \\ &\sum_{i,j,k,l=1}^{N} \langle E_i^-(\boldsymbol{r_1};t)E_j^+(\boldsymbol{r_1};t)E_k^-(\boldsymbol{r_2};t+\tau)E_l^+(\boldsymbol{r_2};t+\tau)\rangle \end{aligned} \tag{2.34}$$

Due to the unpredictable phase differences between the waves originating from various atoms of a chaotic source, only terms where the field from each atom is multiplied with its complex conjugate will survive [72, 74]. Therefore, the only surviving terms in the summation are the following: 1. $i = j = k = l$; 2. $i = j, k = l$; 3. $i = l, j = k$.

$$\begin{aligned} G^{(2)}(\boldsymbol{r_1},\boldsymbol{r_2};\tau) = &\sum_{i=1}^{N}\langle E_i^-(\boldsymbol{r_1};t)E_i^-(\boldsymbol{r_2};t+\tau)E_i^+(\boldsymbol{r_2};t+\tau)E_i^+(\boldsymbol{r_1};t)\rangle \\ &+ \sum_{i\neq j}[\langle E_i^-(\boldsymbol{r_1};t)E_j^-(\boldsymbol{r_2};t+\tau)E_j^+(\boldsymbol{r_2};t+\tau)E_i^+(\boldsymbol{r_1};t)\rangle \\ &+ \langle E_i^-(\boldsymbol{r_1};t)E_j^-(\boldsymbol{r_2};t+\tau)E_i^+(\boldsymbol{r_2};t+\tau)E_j^+(\boldsymbol{r_1};t)\rangle]. \end{aligned} \tag{2.35}$$

We consider that all the atoms have equal contributions and write equation (2.36) as

$$\begin{aligned} G^{(2)}(\boldsymbol{r_1},\boldsymbol{r_2};\tau) = &N\langle E_i^-(\boldsymbol{r_1};t)E_i^-(\boldsymbol{r_2};t+\tau)E_i^+(\boldsymbol{r_2};t+\tau)E_i^+(\boldsymbol{r_1};t)\rangle \\ &+ N(N-1)[\langle E_i^-(\boldsymbol{r_1};t)E_j^-(\boldsymbol{r_2};t+\tau)E_j^+(\boldsymbol{r_2};t+\tau)E_i^+(\boldsymbol{r_1};t)\rangle \\ &+ \langle E_i^-(\boldsymbol{r_1};t)E_j^-(\boldsymbol{r_2};t+\tau)E_i^+(\boldsymbol{r_2};t+\tau)E_j^+(\boldsymbol{r_1};t)\rangle]. \end{aligned} \tag{2.36}$$

The factor $N(N-1)$ in the second term on the right-hand side is the number of possible permutations between two different atoms without repetition. If the number of atoms N is very large, the first term on the right-hand side of the above equation can be neglected

[74].

$$\begin{aligned} G^{(2)}(\boldsymbol{r_1}, \boldsymbol{r_2}; \tau) = N^2[&\langle E_i^-(\boldsymbol{r_1}; t) E_j^-(\boldsymbol{r_2}; t+\tau) E_j^+(\boldsymbol{r_2}; t+\tau) E_i^+(\boldsymbol{r_1}; t)\rangle \\ &+ \langle E_i^-(\boldsymbol{r_1}; t) E_j^-(\boldsymbol{r_2}; t+\tau) E_i^+(\boldsymbol{r_2}; t+\tau) E_j^+(\boldsymbol{r_1}; t)\rangle]. \end{aligned} \tag{2.37}$$

Using equations (2.9), one can write the above equation in the familiar form of

$$G^{(2)}(\boldsymbol{r_1}, \boldsymbol{r_2}; \tau) = G^{(1)}(\boldsymbol{r_1}, \boldsymbol{r_1}; 0) G^{(1)}(\boldsymbol{r_2}, \boldsymbol{r_2}; 0) + |G^{(1)}(\boldsymbol{r_1}, \boldsymbol{r_2}; \tau)|^2. \tag{2.38}$$

Hence the above equation can be written in the form of:

$$G^{(2)}(\boldsymbol{r_1}, \boldsymbol{r_2}; \tau) = \langle I(\boldsymbol{r_1}; t)\rangle \langle I(\boldsymbol{r_2}; t+\tau)\rangle + |G^{(1)}(\boldsymbol{r_1}, \boldsymbol{r_2}; \tau)|^2. \tag{2.39}$$

As a result, the second-order degree of coherence can be written as:

$$g^{(2)}(\boldsymbol{r_1}, \boldsymbol{r_2}; \tau) = 1 + |g^{(1)}(\boldsymbol{r_1}, \boldsymbol{r_2}; \tau)|^2. \tag{2.40}$$

The above relation relates the first and second-order degree of coherence for chaotic-thermal light and is known as **Siegert relation** [73, 75]. The Siegert relation can be applied to chaotic light, like the kind that is generated by numerous unconnected scatterers, or in a broader sense, to light whose electric field can be considered as a random variable with a Gaussian probability distribution. However, it should be noted that the Siegert relation is not always applicable. This is particularly evident in the case of laser light, which has a uniform and uncorrelated intensity correlation function. In the case of laser light, the intensity fluctuations are solely caused by shot noise, and the Siegert relation is not a suitable method for analyzing these phenomena [76, 77].

## 2.6 From classical to quantum optics

Up until now, our focus has been on exploring the principles of coherence theory within the framework of classical physics. Now we take a step forward to introduce its quantum counterpart. The discovery of quantum theory completely transformed our understanding of light, leading to a significant change in how we perceive its nature and behavior. The understanding of light and its properties has a long and fascinating history shaped by various debates and discussions. In the past, there were conflicting views on whether light was a wave or a particle. However, the advent of quantum theory provided a solution by suggesting that light possesses both wave-like and particle-like characteristics. This duality is best observed in optics through experiments using beam splitters that highlight the fundamental properties of photons. While classical optics can explain many phenomena, it falls short of fully describing the behavior of light, making quantum optics essential in interpreting those phenomena that cannot be explained classically, such as wave-particle duality of light[74, 78, 79, 80] and quantum entanglement [11].

In the transition from classical to quantum optics, the concept of the electric field is replaced by the concept of the wave function. Let us go back to the double slit experiment pictured in figure 2.1. For a single photon, equation (2.6) will be written as

$$\boldsymbol{\Psi}(\boldsymbol{r};t) = k_1\boldsymbol{\Psi}(\boldsymbol{r_1};t-t_1) + k_2\boldsymbol{\Psi}(\boldsymbol{r_2};t-t_2), \tag{2.41}$$

where $\boldsymbol{\Psi}(\boldsymbol{r};t)$ is the wave function at position $r$ and time $t$, and $k_1$ and $k_2$ are two imaginary constants that depend on the dimensions of the apertures and the geometry of the setup. The probability amplitude at location $r$ is then

$$\begin{aligned}|\boldsymbol{\Psi}(\boldsymbol{r};t)|^2 = |k_1|^2|\boldsymbol{\Psi}(\boldsymbol{r_1};t-t_1)|^2 + |k_2|^2|\boldsymbol{\Psi}(\boldsymbol{r_2};t-t_2)|^2 \\ + 2Re\{k_1^*k_2\boldsymbol{\Psi}^*(\boldsymbol{r_1};t-t_1)\boldsymbol{\Psi}(\boldsymbol{r_2};t-t_2)\}.\end{aligned} \tag{2.42}$$

In practice, the state of a physical system is often not perfectly determined. We may only know that the system is in a state taken from an ensemble, denoted as

$$\{|\Psi_1\rangle, |\Psi_2\rangle, \ldots, |\Psi_n\rangle\}, \tag{2.43}$$

Each state $|\Psi_i\rangle$ has a probability $p_i$ of occurring, subject to the condition that the probabilities sum to unity, $\sum_i p_i = 1$. We refer to this ensemble as a statistical mixture or **mixed state**, with the individual $|\Psi_i\rangle$ being **pure states**. It is worth noting that the pure states need not be mutually orthogonal [81, 82].

The density operator $\rho$ is a useful construct in this context. When the state is pure, it can be represented by a state vector $|\Psi\rangle$, and we define the corresponding density operator (also known as density matrix) as

$$\rho = |\Psi\rangle\langle\Psi|. \tag{2.44}$$

For a mixed state, we have a set of states $|\Psi_l\rangle$ without any specific restrictions. In this case, the density operator is given by

$$\rho \equiv \sum_l p_l|\Psi_l\rangle\langle\Psi_l|. \tag{2.45}$$

Here, the density operator models the uncertainty regarding which of the states $|\Psi_l\rangle$ the system is in, with each $|\Psi_l\rangle$ assigned a weight $p_l$ in the mixture represented by $\rho$.

Furthermore, the density matrix satisfies the following properties:
1. $\rho$ is Hermitian; i.e. $\rho^{\dagger} = \rho$
2. $\rho$ has trace equal to one: $Tr(\rho) = 1$
3. $\rho$ is a non-negative operator; that is, for any vector $|\Psi\rangle$ in the Hilbert space H, we have $\langle\Psi|\rho|\Psi\rangle \geq 0$.

The trace of the density matrix of a mixed quantum state can be computed by summing up the weights assigned to each sub-state, denoted by $p_l$, such that $Tr(\rho) = \sum_l p_l$. Condition 3 demands that all these weights are positive, hence $0 \leq p_l \leq 1$, with $p_l = 1$ indicating a pure state. Consequently, for a mixed state, the value of $Tr(\rho^2)$ is less than 1, while for a pure state, it is equal to 1. This straightforward criterion can be used to ascertain whether a given state is pure or mixed.

The **reduced density matrix** is one of the most profound applications of the density matrix [25]. It serves as a descriptive tool for subsystems of a composite quantum system, which is a system made up of two or more subsystems. Assuming we have two physical systems, A and B, whose state is characterized by a density operator $\rho^{AB}$. The reduced density operator for subsystem A is defined by

$$\rho^{A} \equiv \mathrm{tr}_{B}(\rho^{AB}), \tag{2.46}$$

where $\mathrm{tr}_B$ is a map of operators referred to as the **partial trace** over the system B [25]. Assume $|a_1\rangle$ and $|a_2\rangle$ are any two vectors in the state space of A, and $|b_1\rangle$ and $|b_2\rangle$ are any two vectors in the state space of B; then the partial trace over the system B is defined as

$$\mathrm{tr}_{B}(|a_1\rangle\langle a_2|\otimes|b_1\rangle\langle b_2|) \equiv |a_1\rangle\langle a_2|\mathrm{tr}(|b_1\rangle\langle b_2|). \tag{2.47}$$

As a simple example, suppose that a quantum state is in a bipartite state $\rho^{AB} = \rho^{A} \otimes \rho^{B}$ where $\rho^{A}$ is the density operator for the system A and $\rho^{B}$ is the density operator for the system B. Then:

$$\rho^{A} = tr_{B}(\rho^{A} \otimes \rho^{B}) = \rho^{A} tr_{B}(\rho^{B}) = \rho^{A}. \tag{2.48}$$

Now that we have introduced the density matrix framework as a tool for analyzing quantum systems, in the next section, we use this framework to study one of the mysterious properties of quantum mechanics, known as quantum entanglement.

## 2.7 Entanglement

Quantum entanglement is a phenomenon in quantum mechanics where the state of two or more particles becomes interconnected in such a way that the state of one particle is dependent on the state of the other particle, regardless of the distance between them. Entangled states are interesting due to the presence of correlations that do not have a classical counterpart. This phenomenon is one of the most fascinating and mysterious concepts in the field of quantum mechanics.

We say a composite pure state $|\Psi\rangle_{AB}$ is entangled if and only if it cannot be written as a separable product of each state.

$$|\Psi\rangle_{AB} \neq |\Psi\rangle_A \otimes |\Psi\rangle_B. \tag{2.49}$$

Mixed states are more commonly encountered in practice than pure states. In contrast to pure states, the entanglement of mixed states is no longer equivalent to non-product states. In fact, a mixed state of two systems is considered non-seperable if its density operator cannot be expressed as a sum of products of density operators corresponding to the subsystems [26, 83]; i.e.

$$\rho \neq \sum_i p_i \rho_i^A \otimes \rho_i^B. \tag{2.50}$$

Bell states, also known as EPR pairs, are a particular type of entangled quantum states that have important implications in quantum information and quantum computing. John S. Bell first introduced these states in the 1960s as a way to test for the violation of local realism in quantum mechanics, As explained in the previous chapter [14].

The state $|\Phi^+\rangle = \frac{|00\rangle+|11\rangle}{\sqrt{2}}$ is the most well-known Bell state and is often used as a starting point for discussions about entanglement. It is formed by the two qubits being in the state $|00\rangle + |11\rangle$, which means that both qubits are in a superposition of 0 or 1 and are in the same state. The density operator for the Bell state has the form

$$\begin{aligned} \rho_{AB} &= \left(\frac{|00\rangle + |11\rangle}{\sqrt{2}}\right)\left(\frac{\langle 00|+\langle 11|}{\sqrt{2}}\right) \\ &= \frac{|00\rangle\langle 00|+|11\rangle\langle 00|+|00\rangle\langle 11|+|11\rangle\langle 11|}{2}, \end{aligned} \tag{2.51}$$

where this is a pure state as $Tr(\rho_{AB}^2) = 1$.

The reduced density matrix of the first qubit is found by performing a partial trace over the second qubit

$$\begin{aligned}\rho_A &= \mathrm{tr}_B(\rho_{AB}) \\ &= \frac{|0\rangle\langle 0|\langle 0|0\rangle + |1\rangle\langle 0|\langle 0|1\rangle + |0\rangle\langle 1|\langle 1|0\rangle + |1\rangle\langle 1|\langle 1|1\rangle}{2} \\ &= \frac{|0\rangle\langle 0| + |1\rangle\langle 1|}{2} \\ &= \frac{I}{2}.\end{aligned} \tag{2.52}$$

The reduced density matrix shows a mixed state since $Tr(\frac{I}{2})^2 < 1$. The combined state of two qubits is pure, indicating that we possess complete information about it. Nonetheless, the first qubit is in a mixed state, meaning we lack maximum knowledge about it. This unique attribute, where the joint state of a system is completely known, but a subsystem remains in mixed states, is a noteworthy characteristic of quantum entanglement [25].

A Bell state is known as a maximally entangled state. "Maximally entangled" means that the state of each qubit is maximally mixed, which indicates that the reduced density operator is a multiple of the identity operator [84]. A common way to check whether a pure state is separable or entangled and quantify the degree of entanglement is **Schmidt decomposition**, which is the subject of the next section.

## 2.8 Schmidt decomposition

Exploring composite quantum systems, which are fundamental to quantum computation and quantum information, involves using a broad spectrum of valuable techniques that go beyond density operators and partial trace, including the Schmidt decomposition. The Schmidt decomposition allows us to represent any pure state of a bipartite system as a linear combination of product states with non-negative coefficients, where each product state consists of a state from each subsystem [25, 26, 83, 84, 85].

Suppose $|\Psi\rangle_{AB}$ is a pure state of a composite system, A and B, whose Hilbert spaces have dimensions of m and n. Let $|j\rangle_A$ and $|k\rangle_B$ be any fixed orthonormal bases for systems A and B, respectively. Then $|\Psi\rangle_{AB}$ can be written

$$|\Psi\rangle_{AB} = \sum_{j=1}^{m}\sum_{k=1}^{n} c_{jk}|j\rangle_A|k\rangle_B, \tag{2.53}$$

for some matrix of complex numbers $c_{jk}$ that satisfy $\sum_{jk}|c_{jk}|^2 = 1$ [25, 86]. We consider a general case where the Hilbert spaces of systems A and B have different dimensions. Assuming that $n < m$ and using the singular value decomposition, one can write

$$|\Psi\rangle_{AB} = \sum_{j=1}^{m}\sum_{i=1}^{n}\sum_{k=1}^{n} u_{ji} d_{ii} v_{ik} |j\rangle_A |k\rangle_B, \tag{2.54}$$

where $d$ is a diagonal matrix with non-negative elements, and $u$ and $v$ are unitary matrices. Defining $|i\rangle_A = \sum_{j=1}^{m} u_{ji}|j\rangle_A$ , $|i\rangle_B = \sum_{k=1}^{n} v_{ik}|k\rangle_B$ and $\sqrt{\lambda_i} = d_{ii}$ to find

$$|\Psi\rangle_{AB} = \sum_i \sqrt{\lambda_i}|i\rangle_A|i\rangle_B. \tag{2.55}$$

Equation (2.55) is called the Schmidt decomposition of the state $|\Psi\rangle_{AB}$. Also, $\sqrt{\lambda_i}$ are non-negative real numbers known as **Schmidt coefficients** satisfying the relation $\sum_i \lambda_i = 1$. The set of basis vectors $|i\rangle_A$ and $|i\rangle_B$ constitute the **Schmidt bases** for $A$ and $B$, respectively, and form an orthonormal basis [81, 82, 82, 84, 57, 87, 88]. The effective number of non-zero terms in equation (2.55) is called the **Schmidt number** for the state $|\Psi\rangle_{AB}$. The Schmidt number is a significant attribute of a composite quantum system, which quantifies the degree of entanglement between subsystems $A$ and $B$. When a state is separable, it can be expressed as $|\Psi\rangle_{AB} = |i\rangle_A|i\rangle_B$. Thus, the Schmidt decomposition yields only one term, resulting in a Schmidt number of one. Therefore, a bipartite pure state is entangled if and only if its Schmidt number exceeds one [81, 84].

The density matrix of the pure state $|\Psi\rangle_{AB}$ is written as [87, 88]

$$\rho^{AB} = \sum_i \lambda_i |i\rangle_A|i\rangle_{BB}\langle i|_A\langle i|. \tag{2.56}$$

From (2.56) we find the reduced density matrix for the mixed subsystems A and B as $\rho^A = \sum_i \lambda_i |i\rangle_{AA}\langle i|$ and $\rho^B = \sum_i \lambda_i |i\rangle_{BB}\langle i|$. As shown, the eigenvalues of the two subsystems are the same, and the Schmidt basis is the eigenvectors of the reduced density matrix [57, 87, 88].

Now that we have established a formalism to describe an entangled quantum state, we next explore how such states can be generated by nonlinear optics. In the following section, we will provide an overview of nonlinear processes and examine the features of nonlinear optical materials that enable the creation of entangled quantum states.

## 2.9 Basic introduction to nonlinear optics

Nonlinear optics is concerned with the study of the interaction between light and materials that exhibit nonlinear response to the electric field of light [27]. We will first explore the relationship between the electric field strength $E(t)$ of an applied optical field and the dipole moment per unit volume, or polarization $P(t)$, of a material system. When the electric field is weak, polarization $P(t)$ grows linearly with respect to the electric field strength, i.e.

$$P(t) = \epsilon_0 \chi^{(1)} E(t), \tag{2.57}$$

where $\chi^{(1)}$ is the linear susceptibility of the medium and $\epsilon_0$ is the permittivity of free space.

For the case of a sufficiently strong electric field, we must write the relation between polarization and the electric field strength as a power series

$$\begin{aligned} P(t) &= \epsilon_0 \chi^{(1)} E(t) + \epsilon_0 \chi^{(2)} E^2(t) + \epsilon_0 \chi^{(3)} E^3(t) + ... \\ &= P^{(1)}(t) + P^{(2)}(t) + P^{(3)}(t) + ..., \end{aligned} \tag{2.58}$$

where $\chi^{(2)}$ and $\chi^{(3)}$ are the second and third-order susceptibility of the medium and $P^{(2)}(t) = \epsilon_0 \chi^{(2)} E^2(t)$ and $P^{(3)}(t) = \epsilon_0 \chi^{(3)} E^3(t)$ are the second and third order polarization. For simplicity, we represented the fields $P(t)$ and $E(t)$ as scalar quantities in equation (2.58). However, it should be noted that if we were to treat the fields as vectors, then the susceptibility $\chi^{(1)}$ would become a second-rank tensor, while $\chi^{(2)}$ would become a third-rank tensor, and so on.

Nonlinear optics provides mechanisms to produce photons in entangled quantum states. One such mechanism is parametric down-conversion, which will be explained in the following section. However, it is essential to discuss the properties of nonlinear optical materials first, as they determine which nonlinear processes will be observed and how. Second-order nonlinear optical interactions can only occur in Non-centrosymmetric crystals, which are crystals that lack inversion symmetry. All the even-ordered nonlinear susceptibilities vanish for the materials that display inversion symmetry (such as liquids, gases, amorphous solids, and many crystals). To demonstrate this fact, we assume a centrosymmetric medium with the nonlinear polarization

$$P(t) = \epsilon_0 \chi^{(2)} E^2(t), \tag{2.59}$$

where the applied field is

$$E(t) = \mathcal{E} \cos(\omega t). \tag{2.60}$$

For a medium that possesses inversion symmetry, if we change the sign of the applied electric field $E(t)$, the sign of the induced polarization $P(t)$ also changes. Therefore, equation (2.59) will have the form

$$-P(t) = \epsilon_0 \chi^{(2)} [-E(t)]^2, \tag{2.61}$$

which means that

$$-P(t) = \epsilon_0 \chi^{(2)} E^2(t). \tag{2.62}$$

By comparing equation (2.59) and (2.62), we conclude that $P(t) = -P(t)$, which only happens if $P(t) = 0$. As a result, in a centrosymmetric medium

$$\chi^{(2)} = 0. \tag{2.63}$$

When crystals have anisotropy, their reaction to electromagnetic fields can vary depending on the direction and polarization in which the fields are propagating. If a material exhibits a different refractive index for distinct polarizations of light propagating in a particular direction, the material is referred to as birefringent. Uniaxial birefringence, the simplest type of birefringence, refers to materials in which only one direction governs optical anisotropy, known as the optic axis. In this case, all other directions perpendicular or at a certain angle to the optic axis are optically equivalent. When the material is rotated around this axis, its optical behavior remains unchanged.

Uniaxial birefringent materials possess two refractive indices for every wavelength, which are known as ordinary and extraordinary. The ordinary ray corresponds to light that is polarized perpendicular to the optic axis and undergoes the ordinary refractive index. On the other hand, the extraordinary ray is governed by the extraordinary refractive index when it is polarized either partially or fully collinear with the optic axis. The effective refractive index of the extraordinary ray depends on the direction of propagation or the wavevector.

In the next section, we will introduce parametric down-conversion, a nonlinear optical process that we can use to generate entangled quantum states of light. Since SPDC is a second-order nonlinear optical process, the nonlinear material must be a non-centrosymmetric crystal. Furthermore, its uniaxial birefringence must be considered in the model of the material.

## 2.10 Spontaneous parametric down conversion

Presently, the most commonly utilized experimental method for generating entangled states is spontaneous parametric down-conversion (SPDC) [28, 29]. SPDC is a process in which a photon field of a high-energy light source, known as the **pump** interacts with

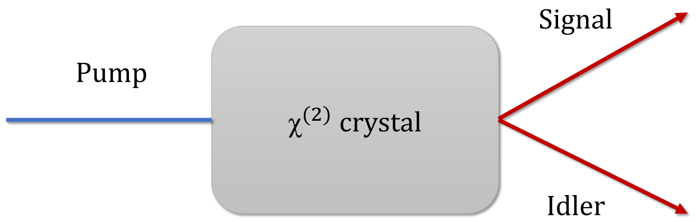

Figure 2.5: Schematic of spontaneous parametric down-conversion in a second-order nonlinear crystal.

a nonlinear medium and splits into two fields of lower energy, referred to as **signal** and **idler**. This phenomenon occurs in non-centrosymmetric crystals when they are illuminated by a high-intensity laser beam. The pump laser operates at a frequency of $\omega_p$, which is typically in the UV or ultraviolet region, whereas the down-converted signal and idler fields have frequencies $\omega_s$ and $\omega_i$ respectively, that are usually in the visible or near infra-red region of the electromagnetic spectrum. "Down-conversion" is a term used to describe the phenomenon where the frequencies of the idler and signal photons are reduced relative to the frequency of the pump photon [27].

The word "Parametric" refers to the fact that the system's quantum mechanical states remain unchanged from the beginning to the end of the process. Consequently, energy is always conserved in parametric processes, whereas it need not be conserved in non-parametric processes as it can be transferred to the crystal medium.

Conservation of momentum, referred to as phase matching condition, is another important principle in SPDC. It refers to the condition where constructive interference of generated waves is achieved in a way that leads to maximum efficiency of the process. Perfect phase-matching is achieved when the wavevector of the incident photon field matches the sum of the wavevectors of the two generated photon fields.

$$\Delta \mathbf{k} = |\mathbf{k}_p - \mathbf{k}_s - \mathbf{k}_i| = 0, \tag{2.64}$$

where $\mathbf{k}_\alpha$ for $\alpha = p, s$, and $i$, refers to the wavevectors of the pump, signal, and idler fields, respectively. Due to energy, momentum, and orbital angular momentum conservation principles, the signal and idler photons become entangled across their temporal, spatial, and angular degrees of freedom.

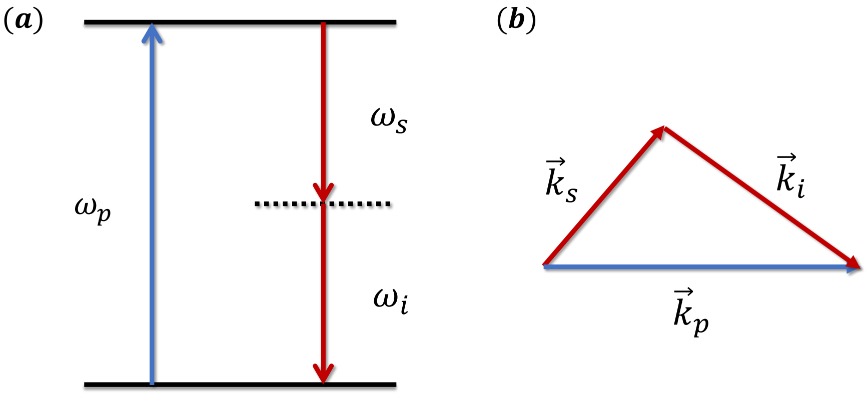

Figure 2.6: (a) Energy-level diagrams describing parametric down-conversion. In SPDC, a pump photon of higher frequency $\omega_p$ annihilates and produces two photons of lower frequencies known as the signal and idler with frequencies of $\omega_s$ and $\omega_i$, respectively. (b) Momentum conservation or phase matching condition in SPDC. The wavevector of the incident photon field $k_p$ matches the sum of the wavevectors of the two generated photon fields $k_s$ and $k_i$.

The use of birefringent crystals is common in nonlinear optical applications to achieve phase matching, and the Beta Barium Borate (BBO) crystal, a uniaxial birefringent crystal with high nonlinearity, is a popular choice for generating SPDC. When the signal and idler photons have the same polarization, the SPDC process is referred to as type-1, while it is known as type-2 if their polarizations are perpendicular [72].

For one specific orientation of the crystal, the emitted signal and idler photons will travel in the same direction as the original pump photon. This phenomenon is referred to as **collinear** emission. However, when the crystal orientation is altered, the signal and idler photons are emitted in different directions as the pump photon due to changes in the phase-matching conditions. This type of emission is known as **non-collinear** emission [72].

The **gain**, which represents the strength of the interaction, increases in direct proportion to the strength of the pump field. The generation of fields in SPDC sources can be characterized by two regimes: the low-gain regime and the high-gain regime. In the low-gain regime, the growth of the generated fields is approximately linear with respect to the pump amplitude, and the output state is a two-photon entangled state. By contrast, the high-gain regime is characterized by the exponential growth of the generated fields with

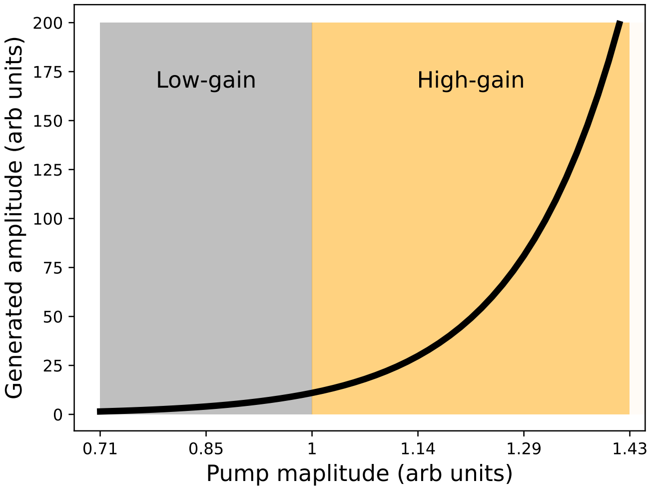

FIGURE 2.7: Generated amplitude as a function of pump amplitude for low and high-gain regimes. In the low-gain regime, the generated fields grow linearly with respect to the pump amplitude, whereas in the high-gain regime, the growth of the generated fields is exponential with respect to the pump amplitude.

respect to the pump amplitude (Fig 2.7), and the output state is a bright, multi-photon entangled state. So far, most research in the field of SPDC has been devoted to studying the low-gain regime. This is mainly because the low gain regime is relatively easy to implement in theoretical models and experimental settings. This emphasis on the low-gain regime has led to significant advancements in our understanding of the phenomenon in this regime [89, 90].

SPDC sources are extensively utilized in fundamental quantum optics experiments such as the violation of Bell's inequality [19, 91], Hong–Ou–Mandel interferometry [92, 93] and quantum technologies such as quantum teleportation [22], quantum cryptography [94], quantum imaging [95], and sub-shot noise imaging [96, 97].

## 2.11 Spatial correlations in SPDC

It is important to accurately determine the correlations of entangled states produced by SPDC as they continue to be the most commonly employed source of entangled states in diverse quantum applications. Over the last few decades, several studies have investigated various temporal and spatial interference effects using the entangled two-photon field generated by SPDC [98, 99, 100, 101], and signal-idler correlation in the spatial domain has been investigated [101, 102, 103, 104, 105].

In the regime of low gain, scientists have extensively investigated the exact form of the two-photon state generated by a general pump profile [106, 54, 53], as well as the Schmidt modes associated with it. The longitudinal phase matching function within the two-photon amplitude is represented by a sinc function [48]. This sinc function gives rise to a distinctive ringed pattern in the far field or momentum space of the two-photon amplitude. Perfect phase matching ($\Delta k_z = 0$) produces a bright central spot with secondary rings surrounding it. The majority of the field's intensity is concentrated within the central region, and it is possible to approximate the phase matching function with a Gaussian function in the case of perfect phase matching [51, 57, 41]. This Gaussian approximation enables an exact Schmidt decomposition using Hermite-Gaussian or Laguerre-Gaussian eigenmodes [49, 51, 57, 50].

The process of generating signal-idler pairs is commonly represented by employing the initial term of a Taylor series. However, when the nonlinear interaction becomes strong, a more complex theoretical approach is necessary. Specifically, the reliability of the Taylor-like series diminishes beyond a few orders because the interaction Hamiltonian does not commute with itself at different times [107, 108]. Therefore, studying SPDC in the high-gain regime has become challenging due to these issues, and high-gain SPDC remains an active and ongoing research area.

Despite extensive research, the influence of pump amplitude on the spatial characteristics of the entangled two-photon state produced in SPDC remains ambiguous. Although some studies suggest the existence of gain-independent Schmidt modes [109, 110], they fail to predict experimentally observed phenomena such as the widening of the angular spectrum of the SPDC field with increasing gain [111, 112].

This thesis aims to theoretically model and experimentally characterize the spatial correlations of entangled fields produced by high-gain SPDC, particularly as a function of input pump amplitude. The spatial correlations will be classified by spatial Schmidt modes, and the resulting Schmidt mode spectrum and Schmidt number will quantify the degree of entanglement between the two fields. Our primary aim is to address the question: How do the Spatial Schmidt modes and their spectrum evolve with respect to increasing gain? In Chapter 3 of this thesis, we outline the theoretical methodology employed for characterizing the spatial Schmidt modes of high gain SPDC as a function of gain. In Chapter 4, we discuss the experimental approach adopted for this study. And finally, in Chapter 5, we will summarize our results and suggest possible avenues for future research.

## 2.12 Summary of the chapter

The current chapter provides an overview of the key concepts used in this work. In section 2.1, we introduced the optical coherence theory, then defined the first-order spatial coherence function in section 2.2. In section 2.3, we discussed the decomposition of the first-order coherence function into coherent modes. We then proceed to introduce the second-order coherence function in section 2.4, which quantifies the correlation between the intensities of two different points in the field. In section 2.5, we explained the Siegert relation, which relates the first and second-order coherence functions for a thermal field.

In section 2.6, we discussed the transition from classical to quantum optics, introduced the necessary formalism to describe the quantum states of light, and highlighted the significance of the density matrix in explaining quantum states that a wave function cannot describe. We introduced the concept of entanglement in section 2.7, which refers to quantum nonlocal correlations with no classical counterpart. In section 2.8, we explained the Schmidt decomposition technique, which is a way of describing an entangled quantum state, and introduced Schmidt modes, spectrum, and Schmidt number, which is a parameter that quantifies the degree of entanglement.

In addition, in section 2.9, we provided an introduction to nonlinear optics, followed by section 2.10, in which we introduced the concept of spontaneous parametric down-conversion (SPDC), a nonlinear process through which entangled states are generated. Finally, in section 2.11, we posed the specific research question that this thesis attempts to address, which is: How do the spatial Schmidt modes and their spectrum evolve as a function of gain in high-gain SPDC?

## Chapter 3

# Theoretical characterization

In the previous chapter, we overviewed the key concepts central to this study. In this chapter, we will explore spatial correlations in high-gain SPDC and use these concepts to characterize them theoretically. We will begin by exploring the theory and methods for expressing squeezed light generated in the SPDC process. Squeezed states of light are characterized by reduced noise below the shot noise limit in one quadrature but at the expense of increased noise in the other quadrature, [55]. Squeezed states have been used in various applications, such as imaging [113, 114, 97] and nonlinear interferometry [115, 116]. One of the most famous applications of squeezed light is in improving the measurement sensitivity of LIGO, a laser interferometer built for detecting gravitational waves [56].

In our analysis, we assume that the signal field is quasi-homogeneous and rotationally symmetric, which allows us to significantly speed up our simulations compared to previous studies. We then perform a coherent mode decomposition on the first-order spatial coherence function to determine the spatial Schmidt modes and Schmidt spectrum. Finally, we track the evolution of the modes and the spectrum as the gain increases. In addition, we quantify the change in the Schmidt number, which represents the degree of entanglement, as a function of gain. Overall, this chapter will provide a theoretical characterization of SPDC in the high-gain regime.

## 3.1 Introduction to squeezed states of light

The quantization of the electromagnetic field is a fundamental principle in quantum electrodynamics, which was proposed by Albert Einstein in 1905 in his explanation of the photoelectric effect [117]. Later, in 1927, Dirac further developed the theory by expanding the electromagnetic field in terms of normal modes. He showed that each mode behaves similarly to a quantum harmonic oscillator with discrete energy levels, where each level corresponds to a specific amount of energy associated with a photon. The energy of a photon can be determined by the equation E $= \hbar\omega$, where $\hbar$ is Planck's constant and $\omega$ represents the frequency of the mode [118].

To mathematically describe the quantization of the electromagnetic field, one can employ creation and annihilation operators. These operators allow for the creation and destruction of photons in a given mode of the electromagnetic field. They correspond to raising and lowering operators for the harmonic oscillators associated with each mode that can increase or decrease the eigenvalue of the modes. The creation operator is typically denoted by $\hat{a}^\dagger$, while the annihilation operator is denoted by $\hat{a}$. By utilizing these operators, the electric field operator can be expressed as [9, 52]

$$\begin{aligned}\hat{E}(\boldsymbol{r};t) &= \hat{E}^{+}(\boldsymbol{r};t) + \hat{E}^{-}(\boldsymbol{r};t) \\ &= \sum_{\mathbf{k}} i\sqrt{\frac{\hbar\omega_k}{2\epsilon_0 V}}\hat{a}(\mathbf{k},t)e^{i(\mathbf{k}.\mathbf{r}-\omega_k t)} - i\sqrt{\frac{\hbar\omega_k}{2\epsilon_0 V}}\hat{a}^\dagger(\mathbf{k},t)e^{-i(\mathbf{k}.\mathbf{r}-\omega_k t)},\end{aligned} \tag{3.1}$$

where $\hat{E}^{+}(\boldsymbol{r};t)$ and $\hat{E}^{-}(\boldsymbol{r};t)$ are positive and negative complex analytic signal operators of the field, respectively. $\mathbf{k}$ and $\omega_k$ denote wave-vector and frequency of the modes, respectively and $V$ is the quantization volume. $\hat{a}$ and $\hat{a}^\dagger$ obey the commutation relation of

$$[\hat{a}, \hat{a}^\dagger] = \hat{a}\hat{a}^\dagger - \hat{a}^\dagger\hat{a} = 1. \tag{3.2}$$

Quadrature operators are defined in the form [119]

$$\hat{X}_1 = \frac{1}{2}(\hat{a} + \hat{a}^\dagger), \tag{3.3a}$$

$$\hat{X}_2 = \frac{1}{2i}(\hat{a} - \hat{a}^\dagger). \tag{3.3b}$$

By using the above definitions, the field operator can be reformulated as

$$\hat{E}(\boldsymbol{r};t) = \sum_{\mathbf{k}} 2i\sqrt{\frac{\hbar\omega_k}{2\epsilon_0 V}}[\hat{X}_1 cos(\phi) + \hat{X}_2 sin(\phi)], \tag{3.4}$$

where $\phi = \mathbf{k}.\mathbf{r} - \omega_k t$. It is clear that $X_1$ and $X_2$ are associated with the field amplitudes oscillating out of phase by $\pi/2$.

The Hermitian operators $X_1$ and $X_2$ correspond to observables, indicating that they can be measured. They are fundamentally without dimensions and relate to position and momentum operators as [120]

$$\hat{x} = \frac{\sqrt{2\hbar/m\omega}}{2}(\hat{a} + \hat{a}^\dagger), \tag{3.5a}$$

$$\hat{p} = \frac{\sqrt{2\hbar m\omega}}{2i}(\hat{a} - \hat{a}^\dagger). \tag{3.5b}$$

the commutation relation for the field quadratures can be written as

$$[\hat{X}_1, \hat{X}_2] = \frac{i}{2}. \tag{3.6}$$

Therefore, The uncertainty principle for the two amplitudes has the form

$$\Delta\hat{X}_1\Delta\hat{X}_2 \geq \frac{1}{4}. \tag{3.7}$$

A coherent state is a specific quantum state that is the right eigenvector of the annihilation operator $\hat{a}$ with eigenvalues $\alpha$

$$\hat{a}|\alpha\rangle = \alpha|\alpha\rangle. \tag{3.8}$$

The vacuum state $|0\rangle$ is a coherent state with the eigenvalue of 0. The coherent state $|\alpha\rangle$ can be expressed as a linear combination of its Fock basis (photon number state) $|n\rangle$ as

$$|\alpha\rangle = \sum_{n=0}^{\infty} \frac{\alpha^n}{\sqrt{n!}} e^{-|\alpha|^2/2}|n\rangle. \tag{3.9}$$

The action of creation and annihilation operators on the photon number states are defined as

$$\hat{a}^\dagger|n\rangle = \sqrt{n+1}|n+1\rangle, \tag{3.10a}$$

$$\hat{a}|n\rangle = \sqrt{n}|n-1\rangle, \tag{3.10b}$$

$$\hat{a}|0\rangle = 0. \tag{3.10c}$$

One of the remarkable characteristics of a coherent state is that it exhibits minimal uncertainty. This quality results in the equation (3.7) adopting a particular form of [80, 119]

$$\Delta\hat{X}_1\Delta\hat{X}_2 = \frac{1}{4}, \quad \text{for a coherent state.} \tag{3.11}$$

The state of a system is said to be **squeezed** if

$$(\Delta\hat{X}_i)^2 \leq \frac{1}{4}, \tag{3.12}$$

for $i = 1$ or 2. The above relation implies that a squeezed state is a quantum state characterized by reduced uncertainty in one of its quadratures at the expense of increased uncertainty in the other. To better understand squeezing, one can utilize the Wigner function, which is the probability distribution of a quantum system in phase space. In Figure 3.1, the Wigner function is illustrated for the coherent state, vacuum state, and squeezed state.

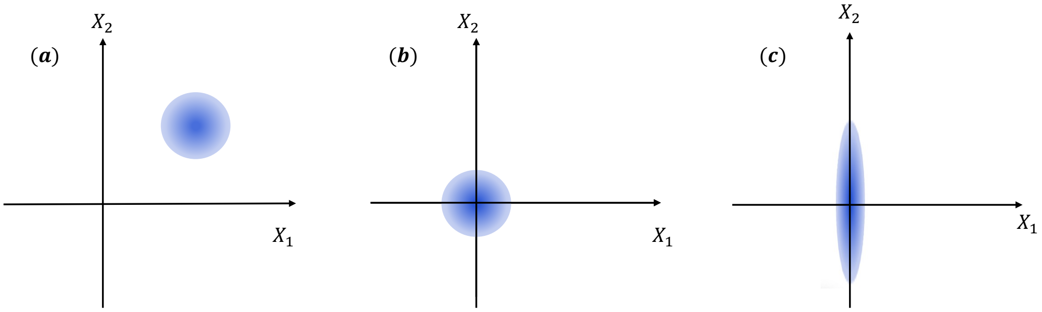

FIGURE 3.1: Wigner function of (a) coherent, (b) vacuum, and (c) squeezed vacuum state. State (c) is a vacuum state squeezed in $X_1$ quadrature. As shown by equation (3.5a), the $X_1$ quadrature corresponds to the position operator; hence the term "position squeezed" is used to describe the state (c).

To understand how squeezing works, consider the state [55, 121]

$$|\Psi\rangle = |0\rangle - \sqrt{2}s|2\rangle, \tag{3.13}$$

where $s$ is a real positive number and the states $|0\rangle$ and $|2\rangle$ represent photon number states. $\langle\Delta X_1^2\rangle$ can be calculated as

$$\langle\Delta X_1^2\rangle = \langle\Psi|\frac{(\hat{a}+\hat{a}^\dagger)^2}{4}|\Psi\rangle. \tag{3.14}$$

If we consider $s$ to be a small number, the above equation will have the form

$$\langle\Delta X_1^2\rangle = \frac{1}{4} - s. \tag{3.15}$$

Hence the first quadrature $X_1$ of the state $|\Psi\rangle$ is squeezed for positive s. Now we repeat this calculation for the second quadrature

$$\langle \Delta X_2^2 \rangle = \langle \Psi | -\frac{(\hat{a} - \hat{a}^\dagger)^2}{4} | \Psi \rangle; \tag{3.16}$$

and we will find that

$$\langle \Delta X_1^2 \rangle = \frac{1}{4} + s. \tag{3.17}$$

Therefore, the second quadrature $X_2$ of the state $|\Psi\rangle$ is expanded for positive s.

Squeezed light can be generated through SPDC. The squeezing of a single mode, such as the aforementioned example, can be achieved through degenerate SPDC, which occurs when the two photons produced are identical in all their attributes, including direction, frequency, and polarization. On the other hand, non-degenerate SPDC can be used to achieve two-mode squeezing [122]. To understand this mechanism, it is necessary to examine the two-mode state. As an example, consider the state

$$|\Psi\rangle = |0\rangle_a \otimes |0\rangle_b - 2s|1\rangle_a \otimes |1\rangle_b, \tag{3.18}$$

where $a$ and $b$ represent signal and idler photons. The squeezing of quantum fluctuations does not occur in the individual modes but rather in a combination of the two modes due to the correlations between them. Therefore, we define the superposition quadrature operators as

$$\hat{X}_1 = \frac{1}{\sqrt{8}}(\hat{a} + \hat{a}^\dagger + \hat{b} + \hat{b}^\dagger), \tag{3.19a}$$

$$\hat{X}_2 = \frac{1}{\sqrt{8}}(\hat{a} - \hat{a}^\dagger + \hat{b} - \hat{b}^\dagger). \tag{3.19b}$$

$\langle \Delta X_1^2 \rangle$ can be calculated as

$$\langle \Delta X_1^2 \rangle = \frac{1}{8} \langle \Psi | (\hat{a} + \hat{a}^\dagger + \hat{b} + \hat{b}^\dagger)^2 | \Psi \rangle. \tag{3.20}$$

We assume that $s$ is a small number, so the above relation will have the form

$$\langle \Delta X_1^2 \rangle = \frac{1}{4} - s. \tag{3.21}$$

The above relation implies that for positive values of s, the two-modes state is squeezed in the modes' $X_1$ quadratures.

The squeezed operator is defined as [119, 121]

$$\hat{S}(\xi) = \exp[\frac{1}{2}(\xi^* a^2 - \xi a^{\dagger 2})], \tag{3.22}$$

where $\xi = re^{i\theta}$ is a complex number with modulus $r$ and argument $\theta$. The state of a two-mode squeezed state is written as [119, 121, 123, 124, 125]

$$|\xi\rangle_2 = \frac{1}{\text{coshr}} \sum_{n=0}^{\infty} (-1)^n e^{in\theta} (\text{tanhr})^n |n, n\rangle, \tag{3.23}$$

where $|n, n\rangle = |n\rangle_a \otimes |n\rangle_b$ indicates the two-mode number states. The density matrix for this state will have the form

$$\rho_{ab} = |\xi\rangle_{22}\langle\xi|, \tag{3.24}$$

and the reduced density matrix for each mode separately is found to be

$$\rho_a = \sum_{n=0}^{\infty} \frac{\tanh^{2n}(r)}{\cosh^2(r)} |n\rangle_{aa}\langle n|. \tag{3.25}$$

One can rewrite the above equation as

$$\rho_a = \sum_{n=0}^{\infty} \frac{\langle n\rangle^n}{(1 + \langle n\rangle)^{n+1}} |n\rangle_{aa}\langle n|, \tag{3.26}$$

with $\langle n\rangle = \sinh^2(r)$ representing the average photon number. The above equation corresponds to the Bose-Einstein distribution, which describes a thermal field [74, 80, 126]. This result implies that the photon statistics of each individual mode in a two-mode squeezed vacuum is identical to that of a single-mode thermal field [119, 123, 126].

The focus of our work is on the global entangled state of the signal and idler fields generated through non-degenerate high-gain SPDC, which is a bipartite multimode squeezed state [122, 127]. For this case, equation (3.26) can be generalized to infer that each of the twin beams of signal and idler generated through high gain SPDC obey photon statistics equivalent to that of a multimode thermal field [109, 128, 127]. In section 2.5, we explained that the Siegert relation (equation (2.39)) shows that for a thermal field, the first and second-order coherence functions are related. Typically, the first-order coherence function is measured through interferometry, but in our case, we simplify the task by exploiting the thermal nature of the signal field. We can measure the second-order spatial coherence function $G^{(2)}(\boldsymbol{q}, \boldsymbol{q'})$ from the statistics of signal field's intensity fluctuations and infer the first-order spatial coherence function $G^{(1)}(\boldsymbol{q}, \boldsymbol{q'})$ from it and then perform an eigen-decomposition on $G^{(1)}(\boldsymbol{q}, \boldsymbol{q'})$ to find the Schmidt modes. In the following section, we demonstrate that the coherent modes of the first-order coherence function of the signal field are equivalent to the global Schmidt modes of the entangled field.

## 3.2 Equivalence between global Schmidt modes and local eigenmodes

One of the main focuses of this thesis is to tackle the challenge of breaking down the two-photon field $|\Psi(\boldsymbol{q}_s, \boldsymbol{q}_i)\rangle$ into its corresponding Schmidt modes, $u_j(\boldsymbol{q}_s)$ and $v_j(\boldsymbol{q}_i)$

$$|\Psi(\boldsymbol{q}_s, \boldsymbol{q}_i)\rangle = \sum_j \sqrt{\lambda_j} |u_j(\boldsymbol{q}_s)\rangle |v_j(\boldsymbol{q}_i)\rangle, \tag{3.27}$$

where $\boldsymbol{q}_s$ and $\boldsymbol{q}_i$ are the transverse wave vectors of the signal and idler fields. The reduced density matrix of the individual signal field can be written as

$$\rho_s = Tr_i(|\Psi(\boldsymbol{q}_s, \boldsymbol{q}_i)\rangle\langle\Psi(\boldsymbol{q}_s, \boldsymbol{q}_i)|) = \sum_j \lambda_j |u_j(\boldsymbol{q}_s)\rangle\langle u_j(\boldsymbol{q}_s)|, \tag{3.28}$$

where $|u_j(\boldsymbol{q}_s)\rangle$ are the spatial Schmidt modes of the signal field. The reduced one-particle density matrix $\rho_s$ and the first-order spatial correlation function $G^{(1)}(\boldsymbol{q}, \boldsymbol{q'})$ ( equation (2.17)) convey equivalent information [129, 130]. The relationship between the first-order correlation function and the reduced one-particle density matrix is formally defined as

$$G^{(1)}(\boldsymbol{q}, \boldsymbol{q'}) = \langle \boldsymbol{q}|\rho_s|\boldsymbol{q'}\rangle. \tag{3.29}$$

As discussed in section 2.3, The first-order spatial correlation function admits the coherent mode representation of

$$G^{(1)}(\boldsymbol{q}, \boldsymbol{q'}) = \sum_j \lambda_j u_j^*(\boldsymbol{q}) u_j(\boldsymbol{q'}). \tag{3.30}$$

Equations (3.28) and (3.30 )represent the same physical concept. As a result, one can construct the spatial Schmidt modes of the two field systems by performing a coherent mode decomposition on the spatial first-order correlation function of one of the fields taken separately. Furthermore, the effective number of coherent modes represents the Schmidt number and can be found by

$$K = \frac{(\sum \lambda_j)^2}{\sum \lambda_j^2}, \tag{3.31}$$

where the numerator is equal to one since the Schmidt coefficients satisfy the relation $\sum_i \lambda_i = 1$.

Having established that the coherent modes of the first-order coherence function of the signal field are equal to the global Schmidt modes of the entangled field, our focus now shifts to expressing the first-order coherence function for the high-gain SPDC. In the following section, we introduce the model that we have adopted to describe high-gain SPDC and examine the assumptions and conditions underlying it.

## 3.3 Theoretical Model of SPDC

The interaction Hamiltonian of PDC is [52, 54, 131]

$$H(t) = \frac{\epsilon_0}{2}\int_V d^3\boldsymbol{r}\chi^{(2)}\boldsymbol{E}_p(\boldsymbol{r},t)\boldsymbol{E}_i(\boldsymbol{r},t)\boldsymbol{E}_s(\boldsymbol{r},t); \tag{3.32}$$

where $\hat{\boldsymbol{E}}_j(\boldsymbol{r},t)$ for $j = p, s$, and $i$ represents the electric field of the pump, signal, and idler fields, respectively, and $V$ is the interaction volume inside the nonlinear crystal. By using equation (3.1), it is possible to represent $\hat{\boldsymbol{E}}_j(\boldsymbol{r},t)$ as a sum of its positive and negative frequency field operators. This sum involves eight terms corresponding to combinations of the positive and negative-frequency field operators. However, only the two terms that conserve energy survive, while the other six terms average out to zero when $\hat{H}$ is integrated over time. Therefore

$$\hat{H}(t) = \frac{\epsilon_0}{2}\int_V d^3\boldsymbol{r}\chi^{(2)}\hat{E}_p^{(+)}(\boldsymbol{r},t)\hat{E}_s^{(-)}(\boldsymbol{r},t)\hat{E}_i^{(-)}(\boldsymbol{r},t) + \text{H.c.}; \tag{3.33}$$

where H.c. represents the Hermitian conjugate of the first term in the above equation. $\hat{E}_j^{(+)}(\boldsymbol{r},t)$ and $\hat{E}_j^{(-)}(\boldsymbol{r},t)$ operators can be expanded in plane-wave representation as

$$\hat{E}_p^{(+)}(\boldsymbol{r},t) = \int C_p d^3\boldsymbol{k}_p A(\boldsymbol{k}_p)e^{i(\boldsymbol{k}_p.\boldsymbol{r}-\omega_p t)}, \tag{3.34a}$$

$$\hat{E}_s^{(-)}(\boldsymbol{r},t) = \int C_s^* d^3\boldsymbol{k}_s \hat{a}_s^\dagger(\boldsymbol{k}_s)e^{-i(\boldsymbol{k}_s.\boldsymbol{r}-\omega_s t)}, \tag{3.34b}$$

$$\hat{E}_i^{(-)}(\boldsymbol{r},t) = \int C_i^* d^3\boldsymbol{k}_i \hat{a}_i^\dagger(\boldsymbol{k}_i)e^{-i(\boldsymbol{k}_i.\boldsymbol{r}-\omega_i t)}. \tag{3.34c}$$

The coefficients $C_j$ vary with frequency but change gradually within the frequency range relevant to most down-conversion experiments. The wavevector $\boldsymbol{k}_j = (\boldsymbol{q}_j, k_{jz})$ corresponds to the generated field, with $\boldsymbol{q}_j$ and $k_{jz}$ representing the transverse and longitudinal wavevectors, respectively. The position vector $\boldsymbol{r} = (\boldsymbol{\rho}, z)$ specifies the location in space, where $\boldsymbol{\rho}$ denotes the transverse coordinate within the cross-section of the pump beam. Furthermore, the Fourier amplitude of the pump, $A(\boldsymbol{k}_p)$, is assumed to be strong enough to be treated classically (Parametric approximation).

Substituting equations (3.34) into equation (3.33)

$$\hat{H}(t) = \frac{\epsilon_0 \chi^{(2)} C_p C_s^* C_i^*}{2} \int_V d^3\boldsymbol{r} \int\int\int d^3\boldsymbol{k}_p d^3\boldsymbol{k}_s d^3\boldsymbol{k}_i A(\boldsymbol{k}_p)\hat{a}_i^\dagger(\boldsymbol{k}_i)\hat{a}_s^\dagger(\boldsymbol{k}_s) \\ e^{i(\boldsymbol{k}_p-\boldsymbol{k}_s-\boldsymbol{k}_i).\boldsymbol{r}} e^{-i(\omega_p-\omega_s-\omega_i).t} + \text{H.c.} \tag{3.35}$$

The two-photon field is initially prepared in a vacuum state with no photons in either the signal or the idler mode at time $t = -t_{\text{int}}$. This state is represented as $|\Psi(-t_{\text{int}})\rangle = |\text{vac}\rangle_s|\text{vac}\rangle_i$. At the time $t = 0$, the state of the two-photon field is to be determined as

$$|\Psi(0)\rangle = \exp(-\frac{i}{\hbar}\int_{-t_{int}}^{0} dt\hat{H}(t))|0\rangle_s|0\rangle_i. \tag{3.36}$$

If we consider the parametric interaction to be weak, we can use the first two terms of the perturbative expansion to approximate the above equation.

The first-order spatial correlation function in the low-gain regime can be written as [90]

$$G^{(1)}(\boldsymbol{q},\boldsymbol{q}') = \frac{k_{arb}}{k_{sz}k'_{sz}} \int d\boldsymbol{q}_i \langle A'(\boldsymbol{q}_s+\boldsymbol{q}_i)A'^*(\boldsymbol{q'}_s+\boldsymbol{q}_i)\rangle \\ \times \text{sinc}(\Delta k_z L/2)\text{sinc}(\Delta k'_z L/2)e^{i(\Delta k_z-\Delta k'_z)L/2}. \tag{3.37}$$

The quantity $k_{arb}$ is an overall scaling factor, and L is the length of the nonlinear crystal.

In cases where the pump power is high, the above perturbative approach is not applicable, and comprehensive theoretical characterization of high-gain SPDC remains an active research area. Analytical expression of the output state has been formulated for spatial cases such as the plane-wave pump [132, 133]; however, existing theoretical models are limited in their ability to describe the correlation function for a general pump field. Here we follow the theoretical description presented in reference [90], which models SPDC in a classical framework in both low and high-gain regimes for a narrow-band pump, where the angular and frequency bandwidths of the pump ($\delta q_p$ and $\delta\omega_p$) are much narrower than the corresponding bandwidths of the generated SPDC field ($\delta q_s$ and $\delta\omega_s$).

In the high-gain regime, the first-order correlation function for a narrow-band pump will have the form [90]

$$G^{(1)}(\boldsymbol{q_s}, \boldsymbol{q_s}') = \frac{k_{arb}}{k_{sz}k'_{sz}} \int d\boldsymbol{\rho} \langle |V_p(\boldsymbol{\rho})|^2 \rangle e^{-i(\boldsymbol{q}_s - \boldsymbol{q'}_s)\boldsymbol{\rho}} \\ \times \frac{\sinh[\Gamma(\Delta\bar{k}_z, \boldsymbol{\rho})L]}{\Gamma(\Delta\bar{k}_z, \boldsymbol{\rho})} \frac{\sinh[\Gamma(\Delta\bar{k}'_z, \boldsymbol{\rho})L]}{\Gamma(\Delta\bar{k}'_z, \boldsymbol{\rho})} e^{i(\Delta\bar{k}_z - \Delta\bar{k}'_z)L/2}, \quad (3.38)$$

where $V_p(\boldsymbol{\rho})$ is the pump beam's spatial profile at the crystal's input face, and $\boldsymbol{\rho}$ is the transverse position. In our experiment, the pump field has a Gaussian profile.

$$V_p(\boldsymbol{\rho}) = g e^{-|\boldsymbol{\rho}|^2/w_p^2}, \quad (3.39)$$

where g is a pump amplitude scaling factor and $w_p$ indicates the beam-waist of the pump. Also,

$$\Gamma(\Delta\bar{k}_z, \boldsymbol{\rho}) \equiv \sqrt{Q^2(\boldsymbol{\rho}) - (\frac{\Delta\bar{k}_z}{2})^2}, \quad (3.40)$$

in which

$$Q^2(\boldsymbol{\rho}) = \frac{4d_{\text{eff}}^2 \omega^2 \omega'^2}{k_{sz}k'_{sz}c^4} |V_p(\boldsymbol{\rho})|^2, \quad (3.41)$$

where $d_{\text{eff}} = \frac{\chi^{(2)}}{2}$ is the nonlinear coupling coefficient of the crystal medium and $\omega$ is the frequency of the generated field. The intensity pattern of the signal field generated through high-gain SPDC can be found by setting $\boldsymbol{q} = \boldsymbol{q'}$ in equation (3.38)

$$I_s(\boldsymbol{q}) = \frac{k_{arb}}{k_{sz}^2} \int d\boldsymbol{\rho} \langle |V_p(\boldsymbol{\rho})|^2 \rangle \left[ \frac{\sinh[\Gamma(\Delta\bar{k}_z, \boldsymbol{\rho})L]}{\Gamma(\Delta\bar{k}_z, \boldsymbol{\rho})} \right]^2. \quad (3.42)$$

We are making an assumption of the narrow-band pump, where the angular and frequency bandwidths ($\delta\boldsymbol{q}_p$ and $\delta\omega_p$) of the pump are significantly smaller than the corresponding bandwidths ($\delta\boldsymbol{q}_s$ and $\delta\omega_s$) of the generated SPDC field. This assumption implies that the variation of the wavevector $\delta k_z$ with respect to $\boldsymbol{q}_p$ (pump wavevector) and $\omega_s$ (pump frequency) is much slower compared to the variation of $A_p(\boldsymbol{q}_p, \omega_p)$, which is typically highly peaked around the central wavevector $\boldsymbol{q}_{p0} = 0$ and the central pump frequency $\omega_{p0}$. Consequently, we can define $\Delta\bar{k}_z$ as the central value of $\Delta k_z$, evaluated for the conditions $q_s + q_i = 0$ and $\omega_s + \omega_i = \omega_{p0}$. It is important to note that this approximation of $\Delta\bar{k}_z \approx \Delta k_z$ holds true only for the specific case of a monochromatic plane-wave pump.

When the pump power is low in a narrow-band pump, the values of $\Gamma(\Delta\bar{k}_z, \boldsymbol{\rho})$ in equation (3.40) is given by $\Gamma(\Delta\bar{k}_z, \boldsymbol{\rho}) = i(\frac{\Delta\bar{k}_z}{2})$. Moreover, the first-order correlation function for the high-gain regime (equation (3.38)) is almost equivalent to the low-gain regime's $G^{(1)}(\boldsymbol{q}, \boldsymbol{q'})$ (equation (3.37)). This equivalence holds precisely for monochromatic waves

(waves with a single frequency value) where the narrow-band approximation is exactly true.

Let us focus on the high-gain regime. Phase matching is generally given by

$$\Delta\bar{k}_z = k_{pz} - k_{iz} - k_{sz}, \tag{3.43}$$

We are considering a collinear case; therefore, the wave vectors of the pump, signal, and idler are all in the same direction, and the above relation simplifies to

$$\Delta k = \mathbf{k}_p - \mathbf{k}_i - \mathbf{k}_s = \Delta\bar{k}_z. \tag{3.44}$$

where

$$\mathbf{k}_l = 2\pi\frac{n_{lo}}{\lambda_l}, \tag{3.45}$$

where $n_{lo}$ for $l = s, i$ is the value of the ordinary refractive indices of BBO for the signal and idler wavelength, respectively. On the other hand, the pump field is extraordinarily polarized (Type 1 SPDC). As a result, its effective refractive index $\eta_p(\theta_p)$ depends on the angle between the pump propagation direction and the optic axis inside the crystal $\theta_p$. Therefore, for the pump beam, equation (3.45) will have the form

$$\mathbf{k}_p = 2\pi\frac{\eta_p(\theta_p)}{\lambda_p}. \tag{3.46}$$

Ordinary and extraordinary refractive indices for a particular wavelength can be obtained using the Sellmeier relations [134]

$$n_e^2(\lambda) = 2.7405 + \frac{0.0184}{\lambda^2 - 0.0179} - 0.0155\lambda^2, \tag{3.47a}$$

$$n_o^2(\lambda) = 2.3730 + \frac{0.0128}{\lambda^2 - 0.0156} - 0.0044\lambda^2. \tag{3.47b}$$

From equation (3.43), the pump field's refractive index for collinear emission can be calculated as

$$\Delta\bar{k}_z = 0; \tag{3.48}$$

$$\eta_p(\theta_p) = (\frac{n_{io}}{\lambda_i} + \frac{n_{so}}{\lambda_s})\lambda_p. \tag{3.49}$$

Equation (2.3.8) in ref [27] demonstrates the relation between $\eta_p(\theta_p)$ and the angle $\theta_p$

$$\frac{1}{\eta_p(\theta_p)^2} = \frac{\sin^2(\theta_p)}{n_{pe}^2} + \frac{\cos^2(\theta_p)}{n_{po}^2}, \tag{3.50}$$

where $n_{pe}$ and $n_{po}$ are the extraordinary and ordinary refractive indices of the pump field, which can be found from equations (3.47). Substituting $\sin^2(\theta_p) = 1 - \cos^2(\theta_p)$ into the above relation, one can find

$$\sin^2(\theta_p) = \frac{\frac{1}{\eta_p(\theta_p)^2} - \frac{1}{n_{po}^2}}{\frac{1}{n_{pe}^2} - \frac{1}{n_{po}^2}}. \tag{3.51}$$

In our experiment, we are considering a non-degenerate case where the signal and idler have different frequencies. Setting $\lambda_s = 700\text{nm}$, $\lambda_i = 720\text{nm}$ and $\lambda_p = 355\text{nm}$ as the values of signal, idler and pump wavelengths, from equation (3.51 one can find the corresponding angle to be $\theta_p = 32.753°$.

Now that we have an expression for the first-order spatial correlation function $G^{(1)}(\boldsymbol{q}, \boldsymbol{q'})$, our next step is to introduce the method employed to determine the spatial Schmidt modes and spectrum from $G^{(1)}(\boldsymbol{q}, \boldsymbol{q'})$. This will be further discussed in the following section.

## 3.4 Numerical computation of the spatial Schmidt modes and Schmidt spectrum

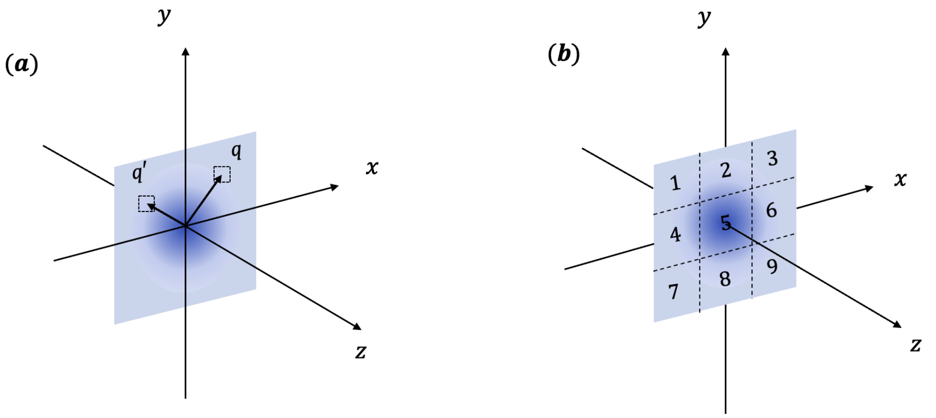

FIGURE 3.2: (a) The light beam's cross-section and selected position vectors $\rho$ and $\rho'$. (b) A simplified schematic to show how the pixels are re-labeled. The cross-section is divided into nine pixels and numbered in row-major order. Here we depicted a simplified version; however, in our analysis of the data, the figures have the dimensions of 256 × 256 pixels. As a result, the cross-section is divided into 256 × 256 × 256 × 256 pixels instead of nine.

In section 3.2, we explained that the spatial Schmidt modes and Schmidt spectrum could be obtained by performing an eigen-decomposition on the first-order correlation function. In the context of the high-gain spontaneous parametric down-conversion

(SPDC) process, the first-order spatial correlation function is given by Equation (3.38). The function $G^{(1)}(\boldsymbol{q}, \boldsymbol{q'})$ is a four-dimensional distribution, which provides information on correlations between complex field amplitude pairs for all points. It depends on four spatial scalar coordinates, two Cartesian coordinates $\boldsymbol{q} = (q_x, q_y)$ for each point, as illustrated in Fig 3.2(a). Although the values can be organized into four-dimensional arrays, analyzing correlations in this form is numerically cumbersome. The method outlined in ref [59] suggests reorganizing the distribution by sequentially numbering transverse-plane points in Fig 3.2(b) and converting the 4D array into a 2D array.

$$G^{(1)}(\boldsymbol{q}, \boldsymbol{q'}) = \begin{pmatrix} G^{(1)}(\boldsymbol{q_1}, \boldsymbol{q_1}) & G^{(1)}(\boldsymbol{q_1}, \boldsymbol{q_2}) & \cdots \\ G^{(1)}(\boldsymbol{q_2}, \boldsymbol{q_1}) & G^{(1)}(\boldsymbol{q_2}, \boldsymbol{q_2}) & \cdots \\ \vdots & \vdots & \ddots \end{pmatrix}. \tag{3.52}$$

The given array comprises rows that correspond to points on the transverse plane and reveal information about the correlation of the field at each point with the field at all other points. The first row exhibits the field's autocorrelation at the first point and its correlation with the field at each subsequent point. The second row displays the correlation of the field at the second point with the field at the first, second, third, and so on. In this manner, each row gives a comprehensive account of the correlations between the field at a particular point and the field at all other points. By restructuring the data in this manner, a 2D representation of the field correlation data is attained for all points on the transverse plane.

If we consider the transverse plane to have dimensions of $N \times M$, the computation of the first-order correlation function can become extremely demanding due to its resulting dimension of $N \times M \times N \times M$. This large dimensionality can pose a significant challenge in terms of processing power, potentially making the computation of the correlation function unfeasible. One option is to reduce the image resolution and analyze a smaller matrix, but this will decrease the precision with which we can track mode evolution as a function of gain.

In our work, we reduce the computational time by exploiting the symmetries of the fields. Specifically, we make the assumption that the signal field is quasi-homogeneous, meaning that the first-order degree of spatial coherence is defined as

$$g^{(1)}(\boldsymbol{q}, \boldsymbol{q'}) = \frac{G^{(1)}(\boldsymbol{q}, \boldsymbol{q'})}{\sqrt{I(\boldsymbol{q})I(\boldsymbol{q'})}}, \tag{3.53}$$

depends only on the distance between two points $\boldsymbol{q}$ and $\boldsymbol{q'}$. In addition, the field generated through SPDC, as depicted in Fig 3.3, exhibits a rotationally symmetric pattern, meaning that its properties are symmetrical with respect to the propagation axis, and

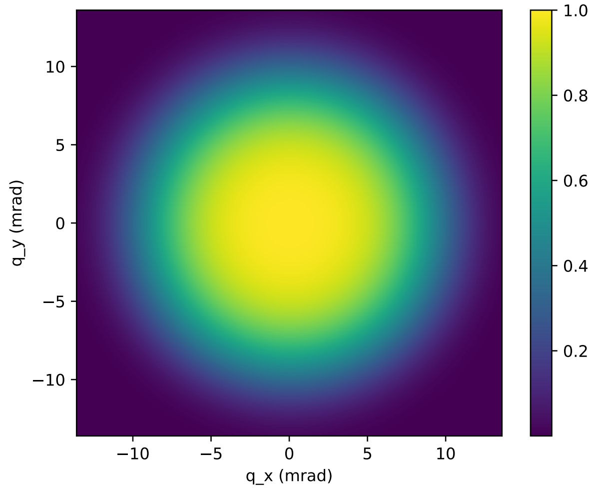

FIGURE 3.3: Simulated normalized average intensity of the signal field generated from high-gain SPDC.

the correlation between two points on the intensity pattern depends only on their radial distance. The rotational symmetry of the signal field can also be deduced from Equation (3.38), taking into account that the pump possesses a Gaussian profile. Moreover, both the first-order correlation function mentioned in Equation (3.38) and the intensity of the Signal described in Equation (3.42) only depend on the radial distance $\boldsymbol{\rho}$. There is no distinction between different directions in space which implies that the x and y coordinates are independent of each other, and we are allowed to factor the correlation function in two Cartesian coordinates, $g^{(1)}(\boldsymbol{q}, \boldsymbol{q'}) = g^{(1)}(\boldsymbol{q}_x, \boldsymbol{q}'_x) g^{(1)}(\boldsymbol{q}_y, \boldsymbol{q}'_y)$. By assuming quasi-homogeneity and rotational symmetry, we can calculate $g^{(1)}(|\boldsymbol{q} - \boldsymbol{q'}|)$ along one direction, such as the x-axis $(\boldsymbol{q}, \boldsymbol{q'} = (q_x = q, q_y = 0; q'_x = q', q'_y = 0))$, thereby dealing with a smaller matrix and eliminating the need for computationally intensive eigen-decomposition of the larger matrix. Our method significantly reduces the computational time compared to previous studies.

Using the rotational symmetry and quasi-homogeneous conditions from equation (3.53), one can approximate the first-order correlation function with

$$G^{(1)}(q, q') \approx g^{(1)}(|q - q'|) \sqrt{I_s(q) I_s(q')}, \tag{3.54}$$

where $I_s(q)$, from equation (3.42), is the signal field's intensity at point $q$ and the correlation function is symmetric as $G^{(1)}(q, q') = G^{(1)}(q', q)$. It is worth noting that the first-order degree of coherence, represented by $g^{(1)}(q', q)$, takes values within the range of $0 \leq g^{(1)}(q', q) \leq 1$, and when $q = q'$, its value is equal to 1. Consequently, in this case,

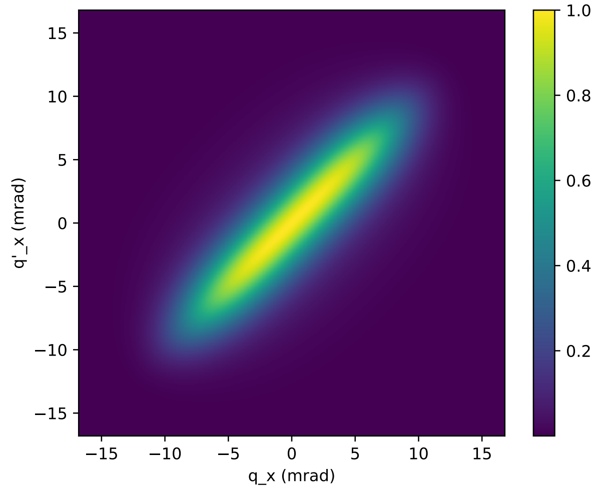

FIGURE 3.4: First-order spatial correlation function $|G^{(1)}(\boldsymbol{q'}, \boldsymbol{q})|$ as a function of transverse wave vector coordinates $q'_x$ and $q_x$.

the correlation function is simplified to $G^{(1)}(q, q) = I_s(q)$. Using equation (3.54), one can visualize the correlation function in two dimensions as depicted in Fig 3.4.

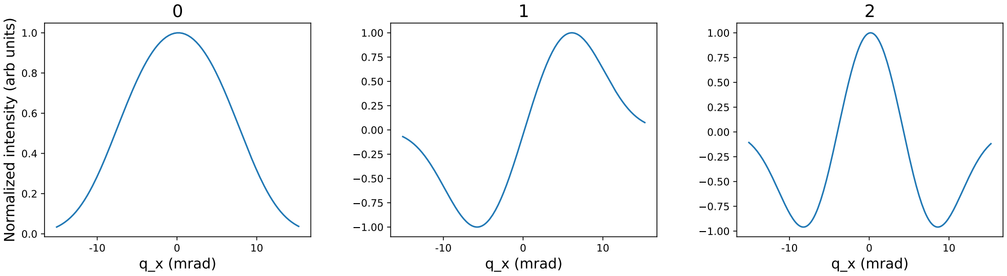

FIGURE 3.5: The real part of simulated one-dimensional spatial Schmidt modes of high gain SPDC. The first-order correlation function of high gain SPDC has been used to compute one-dimensional spatial Schmidt modes. Each plot in the simulation is labeled with a number corresponding to the eigenvector it represents. For instance, the plot labeled "0" represents the $0^{\text{th}}$ eigenvector ($\boldsymbol{\nu_0}$).

To obtain the Schmidt modes and Schmidt spectrum, as explained in section 3.2, we carry out coherent mode decomposition on the 2D correlation function $G^{(1)}(q, q')$ described in equation (3.54)

$$G^{(1)}(q, q') = \sum_j \lambda_j \nu_j^*(q)\nu_j(q'). \tag{3.55}$$

We obtain the Schmidt modes by finding the eigenvectors of the correlation matrix. However, in our calculations, we made the assumption of quasi-homogeneity and rotational symmetry and thus only computed the correlation function along the x-axis direction. As a consequence, the eigenvalues of the correlation function can only give us the Schmidt modes along that specific direction, resulting in one-dimensional modes. The one-dimensional Schmidt modes are illustrated in Figure 3.5. To obtain the two-dimensional modes, we form the tensor product of the one-dimensional modes along the x and y directions. The assumptions of quasi-homogeneity and rotational symmetry imply that the correlation function is identical in all spatial directions, including x and y. Therefore, we reconstructed the two-dimensional Schmidt modes by taking the tensor product of the one-dimensional eigenvectors along the x direction with each other

$$u_{ij} = \nu_i \otimes \nu_j. \tag{3.56}$$

The two-dimensional representation of Schmidt modes is depicted in Fig 3.6. The figure shows that while the signal field has rotational symmetry, the individual modes do not exhibit such a pattern. Nevertheless, the combination of the modes, each multiplied by their respective weights, forms the first-order correlation function, which is rotationally symmetric.

To determine the weight of a two-dimensional mode, we multiply the eigenvalues linked to the eigenvectors utilized to form the mode

$$\lambda_{ij} = \lambda_i \otimes \lambda_j, \tag{3.57}$$

where $\lambda_i$ and $\lambda_j$ are the weights of the $\mathrm{i}^{\mathrm{th}}$ and $\mathrm{j}^{\mathrm{th}}$ eigenvalue and $\lambda_{ij}$ is the weights of the mode $u_{ij}$. Additionally, we reconstructed the Schmidt spectrum by plotting the weights against the mode number, as depicted in Fig 3.7.

## 3.5 Numerical results

In the previous section, we developed a method to extract the Schmidt modes and Schmidt numbers from the intensity profile of the signal field. Next, we apply this method to signal fields generated by various pump strengths. To accomplish this, we utilize our model presented in section 3.2 to predict the first-order correlation function for different pump powers. Subsequently, we utilize our numerical computation system introduced in section 3.4 to predict the corresponding Schmidt modes and numbers that would be observed in an equivalent experiment. To carry out the theoretical characterization, equation (3.38) is utilized to create the first-order correlation function. For numerical analysis, the values

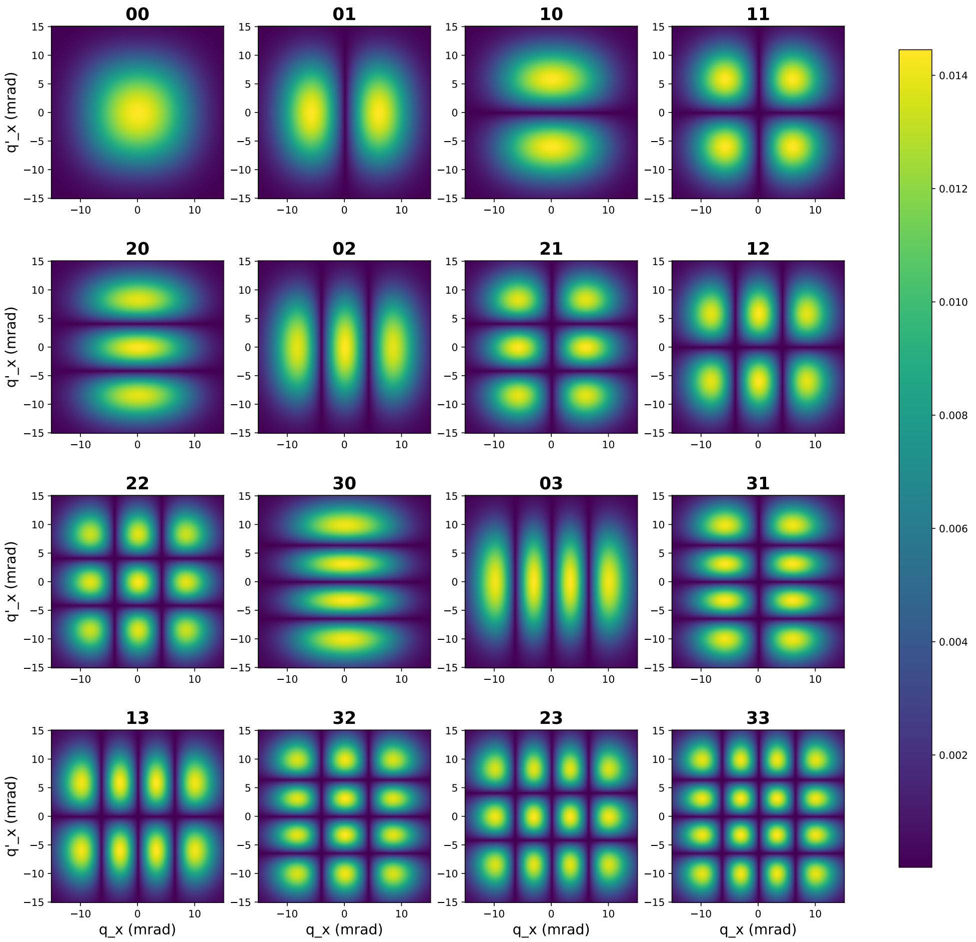

Figure 3.6: The absolute value of simulated two-dimensional spatial Schmidt modes $|u(q'_x, q_x)|$ for high-gain SPDC as a function of transverse wave vector coordinates $q_x$ and $q'_x$. Each mode is a tensor product of a pair of eigenvectors of the first-order correlation function, which are one-dimensional spatial Schmidt modes illustrated in Figure 3.5. The number on top of each plot represents the number of eigenvectors used to construct the mode. For instance, "01" signifies that the mode is the tensor product of the $0^{\text{th}}$ and $1^{\text{st}}$ eigenvectors $(\nu_0 \otimes \nu_1)$. These two-dimensional spatial Schmidt modes have a resemblance to Hermite-Gaussian modes.

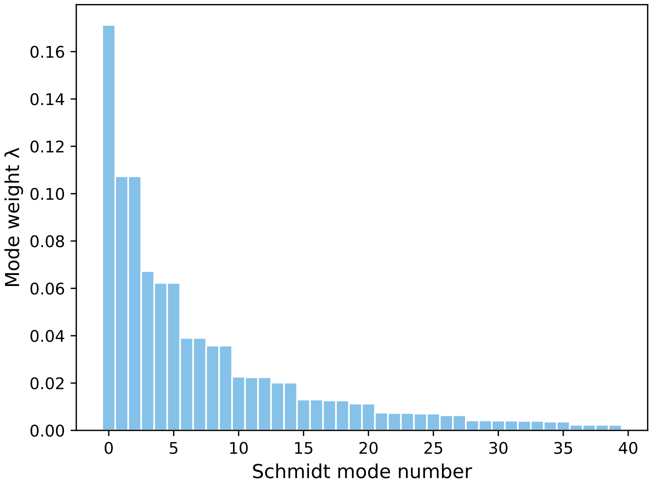

FIGURE 3.7: Schmidt spectrum of high gain SPDC. The weights of the modes $\lambda$ are normalized to their sum up to the 40th mode ($\sum_i^{i=40} \lambda_i$).

of $\lambda_s = 700\text{nm}$, $\lambda_i = 720\text{nm}$ and $\lambda_p = 355\text{nm}$ are chosen for the signal, idler, and pump wavelengths, respectively. The angle between the crystal axis and the pump beam is set to $\theta_p = 32.750°$. The value of $\theta_p$ for the simulations is allowed to have a small deviation from the collinear emission condition $\theta_p^{(coll)} = 32.753°$ because in experiments, $\theta_p$ is set by hand to approximately satisfy collinear emission. We set $L = 3\text{mm}$ and $w_p = 200\mu m$ corresponding to our experimental parameters.

In this study, we examined the spatial Schmidt modes at various amplitudes of the pump, and the results are presented in Fig 3.8. The figure shows the absolute values of four modes, namely 00, 01, 10, and 11, for different gain values of $g$. As the pump amplitude increases, the modes also increase in angular extent. For example, the first mode, mode 00, shows an increase in FWHM from 14.92 mrad to 15.26 mrad to 15.60 mrad as the pump amplitude increases from $g = 1.47$ to $g = 1.56$ to $g = 1.66$ in arbitrary units. To visualize the growth of these modes more clearly, we plotted the cross-sections of the 2-dimensional modes for three different gains in Fig 3.9.

In Fig 3.10, the Schmidt spectrum is shown for two different gain values. The graph demonstrates that as the pump strength increases, the spectrum narrows. Equation (3.31) can be used to compute the Schmidt number, also known as the effective number of modes. A narrower Schmidt spectrum means that fewer effective terms are included in the Schmidt decomposition. Based on the findings presented in figure 3.10, it can be inferred that the spectrum narrows because as the gain increases, the higher-weighted

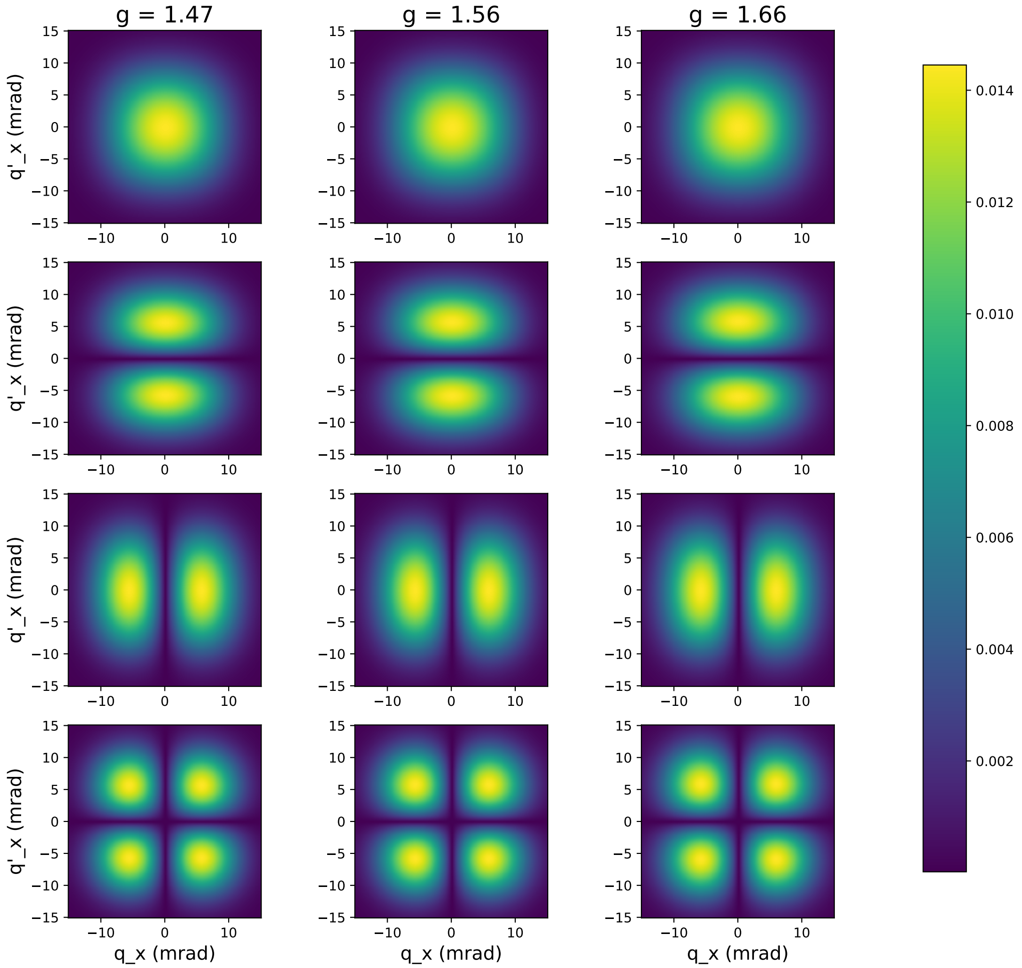

Figure 3.8: The absolute values of simulated two-dimensional spatial Schmidt modes for high gain SPDC, as a function of transverse wave vector coordinates $q_x$ and $q'_x$, across a range of gain values. The modes have been simulated and plotted to demonstrate their behavior under different gain conditions. The first mode 00 shows an increase in FWHM from 14.92 mrad to 15.26 mrad to 15.60 mrad as the pump amplitude increases from $g = 1.47$ to $g = 1.56$ to $g = 1.66$ in arbitrary units.

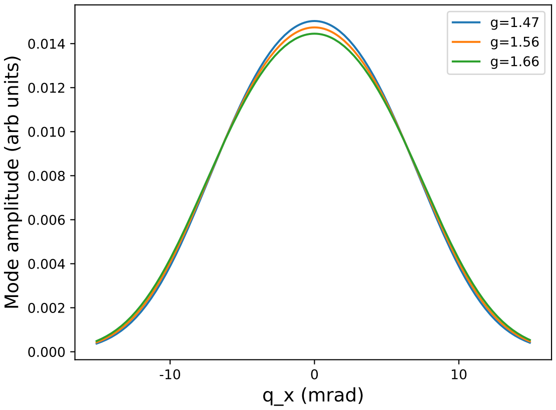

FIGURE 3.9: The cross sections of simulated two-dimensional Spatial Schmidt modes of high gain SPDC for two different gain values. When the pump amplitude (in arb units) increases from $g = 1.47$ to $g = 1.56$ to $g = 1.66$, the full width at half maximum (FWHM) of the mode increases from 14.92 mrad to 15.26 mrad to 15.60 mrad.

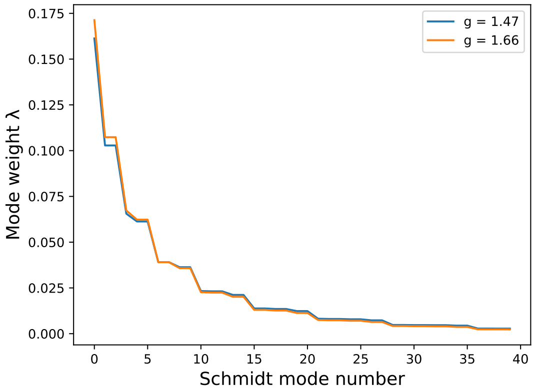

FIGURE 3.10: Simulated Schmidt spectrum for two different values of gain. The spectrum shows a narrowing trend as the pump amplitude increases. This happens because the higher-weighted modes experience more amplification than the lower-weighted modes. The Schmidt number goes from 16.24 to 14.75 when the gain increases from g=1.47 to g=1.66.

modes experience greater amplification compared to the lower-weighted modes. With increasing the gain, the number of effective terms decreases, resulting in a lower Schmidt number. This phenomenon is demonstrated in Figure 3.11. Figure 3.11 demonstrates that as the pump amplitude increases, the degree of the spatial entanglement between signal and idler fields decreases.

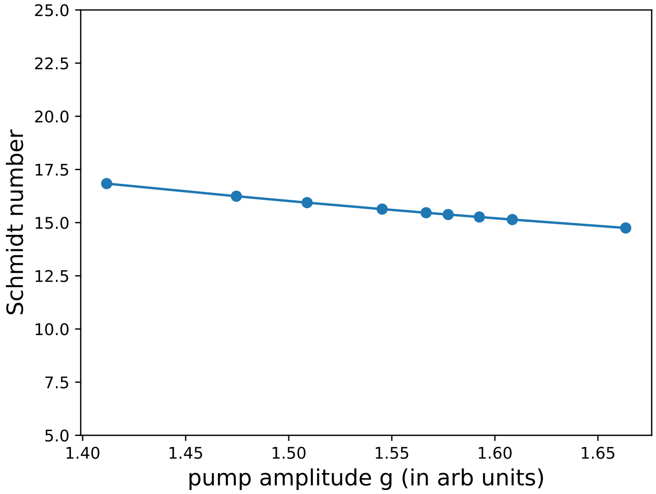

FIGURE 3.11: Evolution of Schmidt number as a function of gain. An increase in gain leads to a decrease in the effective number of modes. In Chapter 2, we discussed that a higher Schmidt number reflects a stronger degree of entanglement between the two fields. In conclusion, the correlations between the two entangled fields weaken as the gain increases.

## 3.6 Summary of the chapter

In this chapter, we provide a theoretical analysis of SPDC, with a particular focus on the high-gain regime. To begin, in section 3.1, we define the signal-idler field as a multi-mode squeezed state and demonstrate that each of the signal and idler fields taken separately follows thermal statistics. In section 3.2, we explore the local eigenmodes of the first-order correlation function of one of the fields and establish their equivalence to the global Schmidt modes of the two-photon state. In section 3.3, we present a theoretical description of the SPDC in the high-gain regime, as well as the expressions for the first-order correlation function in the adopted model. The following section, 3.4, is devoted to introducing the assumptions of statistical homogeneity and rotational symmetry. By utilizing these assumptions, we construct the Schmidt modes and spectrum with significantly greater efficiency than previous methods. In section 3.5, we present numerical results computed for various gain values, predicting that as the pump amplitude increases, the spatial Schmidt modes grow in size while their Schmidt spectrum narrows. As a result, the effective number of modes, or the Schmidt number, decreases as a function of gain. In the next chapter, we will do an experimental investigation to validate the accuracy of our high-gain SPDC model's predictions regarding the Schmidt modes and spectrum.

## Chapter 4

# Experimental characterization of Schmidt modes in high-gain PDC

In this chapter, we focus on experimentally characterizing high-gain SPDC. Previously, we presented a theoretical model that described how the spatial correlation of high-gain SPDC changes as the gain varies. According to our model, increasing gain leads to growth of the Schmidt modes in size, narrowing of the Schmidt spectrum, and a decrease in the Schmidt number, which measures entanglement. In the following, we experimentally test the theoretical predictions derived in the previous chapter. We outline our experimental setup and describe a method for analyzing the data to determine the spatial Schmidt modes and spectrum. Additionally, we investigate how the spatial correlations of high-gain SPDC evolve with increasing gain.

## 4.1 Introduction

As mentioned in section 3.2, the spatial Schmidt modes and spectrum of high-gain SPDC correspond to the eigenvectors and eigenvalues of the first-order correlation function, denoted as $G^{(1)}(\boldsymbol{q}, \boldsymbol{q'})$. In order to investigate the spatial correlations of the SPDC field, it is necessary to measure $G^{(1)}(\boldsymbol{q}, \boldsymbol{q'})$. In section 2.2, it was explained that the first-order spatial correlation function, also referred to as the spatial field correlation, which is closely connected to the phase of the field, is typically measured using interferometry. However, the second-order correlation function, known as the intensity correlation function, can be determined solely by analyzing the statistics of intensity fluctuations for different pairs of points. This can be done using a standard camera capable of capturing images of the light intensity distribution.

In our previous discussion in section 3.1, we explored that the global entangled state of the signal and idler fields generated through non-degenerate high-gain SPDC is a bipartite multimode squeezed state, with each of the individual constituent fields obeying thermal photon statistics. Another concept we examined in section 2.5 is the Siegert relation (equation (2.39)), which relates the first and second-order correlation functions of a thermal field. Specifically, the Siegert relation states that for a thermal field, the second-order correlation function can be expressed in terms of the first-order correlation function as

$$G^{(2)}(\boldsymbol{q},\boldsymbol{q'}) = \langle I(\boldsymbol{q})\rangle\langle I(\boldsymbol{q'})\rangle + |G^{(1)}(\boldsymbol{q},\boldsymbol{q'})|^2. \tag{4.1}$$

Therefore, rather than relying on interferometry to directly measure $G^{(1)}(\boldsymbol{q},\boldsymbol{q'})$, we can instead measure the second-order spatial coherence function and then use the thermal nature of the signal field and the Siegert relation to obtain the first-order spatial coherence function. Hence, the measurement of $G^{(1)}(\boldsymbol{q},\boldsymbol{q'})$ can be achieved through the measurement of the second-order spatial coherence function, which can be obtained from the statistics of intensity fluctuations. Equation (2.27) provides a definition for the second-order coherence function, and by substituting this definition in equation (4.1), we find

$$\langle I(\boldsymbol{q})I(\boldsymbol{q'})\rangle = \langle I(\boldsymbol{q})\rangle\langle I(\boldsymbol{q'})\rangle + |G^{(1)}(\boldsymbol{q},\boldsymbol{q'})|^2. \tag{4.2}$$

The first-order correlation function can be written as

$$\begin{aligned}
|G^{(1)}(\boldsymbol{q},\boldsymbol{q'})| &= \sqrt{\langle I(\boldsymbol{q})I(\boldsymbol{q'})\rangle - \langle I(\boldsymbol{q})\rangle\langle I(\boldsymbol{q'})\rangle} \\
&= \sqrt{\langle I(\boldsymbol{q})I(\boldsymbol{q'})\rangle - \langle I(\boldsymbol{q})\rangle\langle I(\boldsymbol{q'})\rangle + \langle I(\boldsymbol{q})\rangle\langle I(\boldsymbol{q'})\rangle - \langle I(\boldsymbol{q})\rangle\langle I(\boldsymbol{q'})\rangle} \\
&= \sqrt{\langle (I(\boldsymbol{q}) - \langle I(\boldsymbol{q})\rangle)(I(\boldsymbol{q'}) - \langle I(\boldsymbol{q'})\rangle)\rangle} \\
&= \sqrt{\langle \delta I(\boldsymbol{q})\delta I(\boldsymbol{q'})\rangle},
\end{aligned} \tag{4.3}$$

where $\delta I(\boldsymbol{q}) = I(\boldsymbol{q}) - \langle I(\boldsymbol{q})\rangle$. On the right-hand side, we have the square root of the covariance matrix:

$$|G^{(1)}(\boldsymbol{q},\boldsymbol{q'})|= \sqrt{\mathrm{Cov}(I(\boldsymbol{q}),I(\boldsymbol{q'}))}, \tag{4.4}$$

where $\mathrm{Cov}(I(\boldsymbol{q}),I(\boldsymbol{q'})) = \langle \delta I(\boldsymbol{q})\delta I(\boldsymbol{q'})\rangle$ is the covariance matrix. The far-field first-order correlation function, $G^{(1)}(\boldsymbol{q},\boldsymbol{q'})$, and the near-field first-order correlation function, $G^{(1)}_{NF}(\boldsymbol{\rho},\boldsymbol{\rho'})$, are related through a Fourier transform. When a function $z(x)$ exhibits the symmetry property of $z(-x) = z^*(x)$, its Fourier transform becomes a real function (This property is discussed in section 4.1.1 of [64]). In the specific case of SPDC, the pump profile adopts a symmetric Gaussian pattern. For the low-gain regime described by equation (3.37), the phase matching is represented by a sinc function, and its Fourier transform results in a symmetric rectangular function [135]. Similarly, in the high-gain regime (equation (3.38)), the phase matching is represented by $\frac{\sinh[QL]}{Q}$, where $Q = \Gamma(\Delta\bar{k}_z,\boldsymbol{\rho})$. The Fourier transform of this function also yields a symmetric outcome, ensuring that the far-field correlation function remains real. Consequently, determining its absolute value proves sufficient for our analysis.

To determine the first-order correlation function, we need to take multiple images of the signal field's intensity profile and compute the intensity fluctuation using equation (4.4). In the following section, we explain the experimental setup used to acquire images of the signal field's intensity profile for multiple pump amplitudes.

## 4.2 Experimental setup and procedure

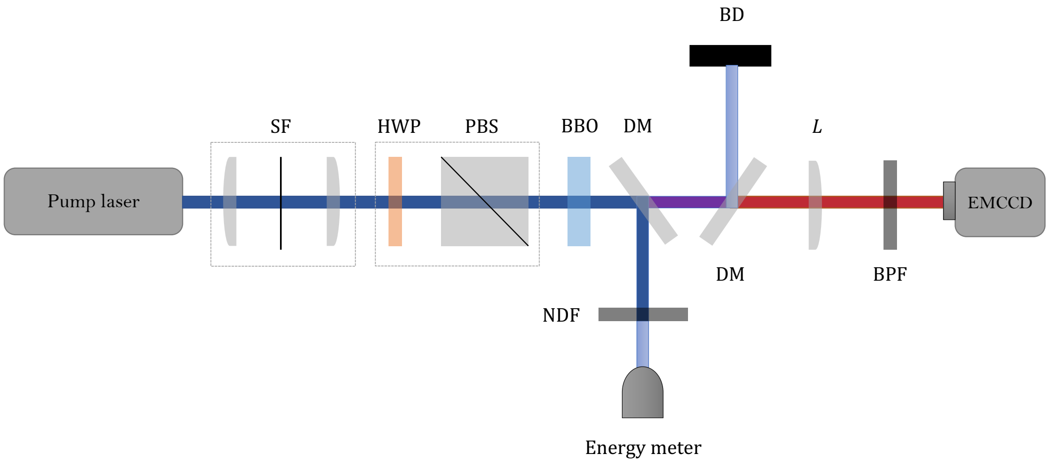

FIGURE 4.1: Schematic of the experimental setup used for measuring the far-field intensity profile in high-gain SPDC for increasing pump strengths. SF: spatial filter, HWP + PBS: half-wave plate + polarizing beam-splitter combination for pump amplitude control, BBO: $\beta$-barium borate nonlinear crystal, DM: dichroic mirror, NDF: Neutral density filter, BD: beam dump, L: Lens with a focal length of 125 cm, BPF: Bandpass filter centered at 700 nm and the FWHM bandwidth of 10 nm to select only the signal field and discard the idler field.

In order to capture the far-field intensity profile in high-gain SPDC with increasing pump strengths, we utilized the setup illustrated in Figure 4.1. The Nd: YAG laser, EKSPLA PL2231, emits 30 ps pulses of vertically-polarized light with a wavelength of 355 nm at a frequency of 50 Hz. The pulses are spatially filtered and then directed towards a 3-mm-long type-I $\beta$-barium borate (BBO) crystal positioned at the pump's waist plane. The crystal is oriented at an angle for which the emission is roughly collinear. A combination of a half-wave plate (HWP) and a polarizing beam-splitter (PBS) is used to control the amplitude of the pump. Modulating the beam intensity can be achieved by adjusting the orientation of the half-wave plate, which in turn alters the polarization of the light that reaches the polarizing beam splitter. Following the crystal, two dichroic mirrors (DM) are employed to remove the pump beam. After the crystal, the initial dichroic mirror directs the remaining pump beam toward the Coherent EnergyMax USB-J-10MB-HE energy meter. Before reaching the energy meter, a Neutral-density filter (NDF) is utilized to reduce the beam's intensity. The energy meter is used to measure the energy of the residual pump beam, and from these measurements, the pump amplitude is measured up to an overall scaling factor. To capture the SPDC far-field, a lens with its focal plane at the crystal output face (125cm) is placed, and the far-field is directly imaged on an Andor Ixon-897 EMCCD camera. A band pass filter centered at the signal wavelength of 700nm and with a bandwidth of 10 nm is positioned at the camera aperture to block the idler field.

We used an EMCCD camera with a pixel size of $16\mu m \times 16\mu m$ to obtain images of the size $256 \times 256$ pixels of the spatial intensity distribution of the signal pulses in high-gain SPDC. The camera had an electron-multiplication gain of 300, and the EMCCD's 0.1 ms acquisition time is triggered by the laser to ensure that each acquired image is a recording of the spatial intensity distribution of only one signal pulse.

## 4.3 Analysis of the experimental data

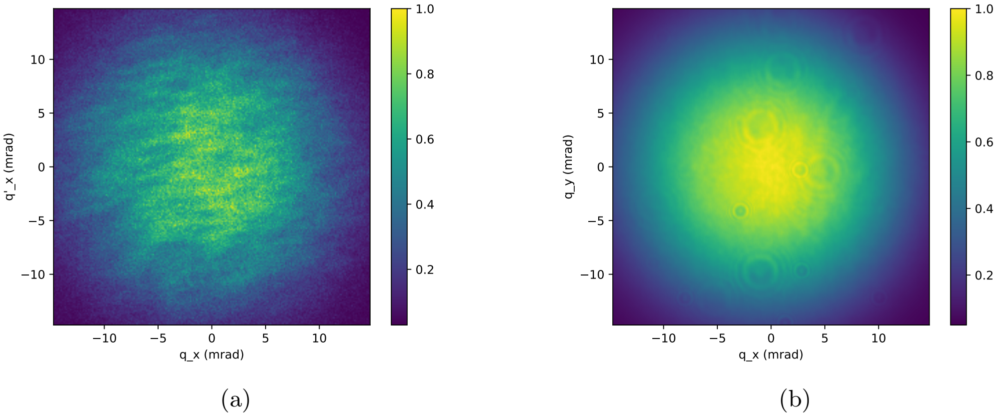

(a)

(b)

FIGURE 4.2: (a) Normalized single shot image of the signal beam obtained from EMCCD camera measurements for a pump amplitude of $g = 1.66$ (arb units). (b) Normalized average intensity profile of the signal beam obtained from EMCCD camera measurements for a pump amplitude of $g = 1.66$ (arb units). The intensity profile is generated by averaging the intensity profile of 5 sets of 1000 single-shot images of the signal field's intensity profile.

In order to obtain the far-field mean intensity distribution, we conducted a series of experiments where we rotated the HWP to different angles to obtain different pump intensities. To account for the statistical error, we took five sets of 1000 single-shot images of the signal field for each corresponding pump amplitude. We also used an energy meter to measure the pulse energy simultaneously. Figure 4.2(a) depicts a normalized single-shot intensity distribution of the signal field, and figure 4.2 illustrates the average intensity distribution of 5 sets of 1000 single-shot images. To account for any fluctuations in pulse-to-pulse power, we normalize each image to the integral intensity.

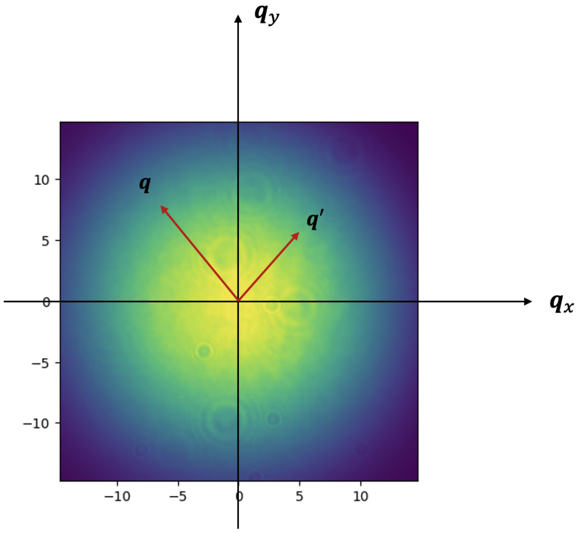

FIGURE 4.3: The correlation function $G^{(2)}(\boldsymbol{q}, \boldsymbol{q'})$ quantifies the intensity correlations between the points labeled by transverse position vectors $\boldsymbol{q}$ and $\boldsymbol{q'}$.

Note from equation (4.4) that we calculate the first-order correlation function using the intensity of two pixels represented by $\boldsymbol{q}$ and $\boldsymbol{q'}$ on the intensity distribution, as shown in Figure 4.3. However, as discussed in section 3.4, due to the two-dimensional nature of the vectors $\boldsymbol{q}$ and $\boldsymbol{q'}$, the resulting first-order correlation function is a four-dimensional matrix, which can be computationally intensive to diagonalize. To simplify the process, similar to the approach discussed in Chapter 3, we center the intensity profile in the images captured using the camera and assume that the signal field is quasi-homogeneous and rotationally symmetric, and calculate the covariance matrix as a function of the distance between the two pixels $G^{(1)}(|\boldsymbol{q} - \boldsymbol{q'}|)$ for a diametric slice $(\boldsymbol{q}, \boldsymbol{q'} = (q_x = q, q_y = 0; q'_x = q', q'_y = 0))$ of the intensity pattern as shown in figure 4.4(a). However, taking a single diametric slice only uses a small portion of the available data. Since we have assumed rotational symmetry, any diametric slice should have the same result, so we can take multiple such slices and average over them to improve the signal-to-noise ratio (Figure 4.4(b)). This results in the first-order correlation function being a two-dimensional function.

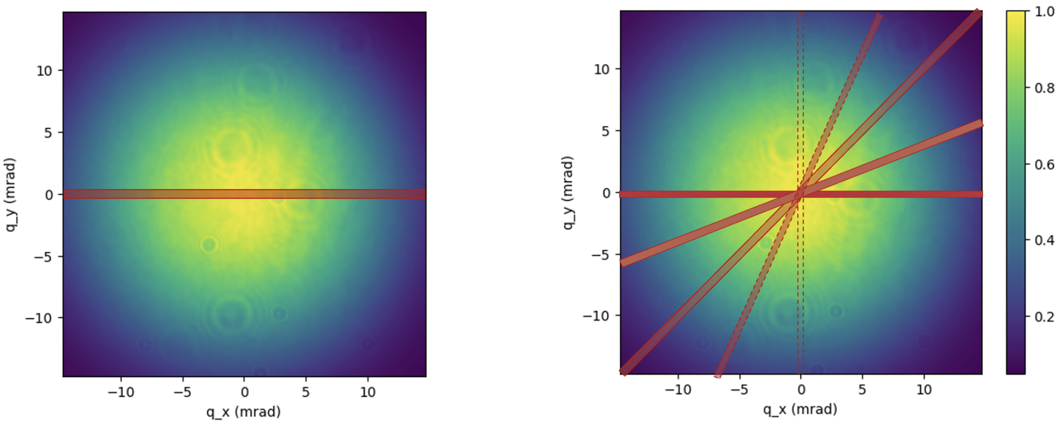

(a) (b)

FIGURE 4.4: (a) In order to optimize the computation, we have decided to compute the covariance function for a single diametric slice of the intensity profile. (b) We compute the average of the covariance function across numerous diametric slices taken at varying angles.

Intensity correlations arise from spatial correlations between photons originating from the same pulse. We anticipate that photons from distinct pulses would be uncorrelated, implying that there should be no correlation between pixels from different images. However, to our surprise, we observed correlations between pixels from different images during the experiment. These correlations, as explained in references [136, 137, 138], are referred to as accidental correlation because their nature is purely accidental. To derive the real spatial correlation between different pixels in each image, we must account for accidental correlation. The accidental correlation can be estimated by calculating the correlations between pixels from the $k^{\text{th}}$ and $k'^{\text{th}}$ images, where $k \neq k'$. By subtracting the accidental correlation from the total correlation, we obtain the real correlation function

$$|G^{(1)}(q,q')| = \frac{1}{N}\sum_{k=1}^{N}\sqrt{\langle \delta I(q)^{(k)}\delta I(q')^{(k)}\rangle} - \frac{1}{N}\sum_{k,k',k\neq k'}^{N}\sqrt{\langle \delta I(q)^{(k)}\delta I(q')^{(k')}\rangle}, \tag{4.5}$$

where the first term indicates the total correlation and the second term is the accidental correlation, and N denotes the total number of images. Figure 4.5 illustrates the process of eliminating the accidental correlation. First, we obtain the single-shot intensity distributions of the signal field using the EMCCD (4.5(a)). Next, we determine the total correlation (4.5(b)) by evaluating the first term in equation 4.5. Then, we compute the

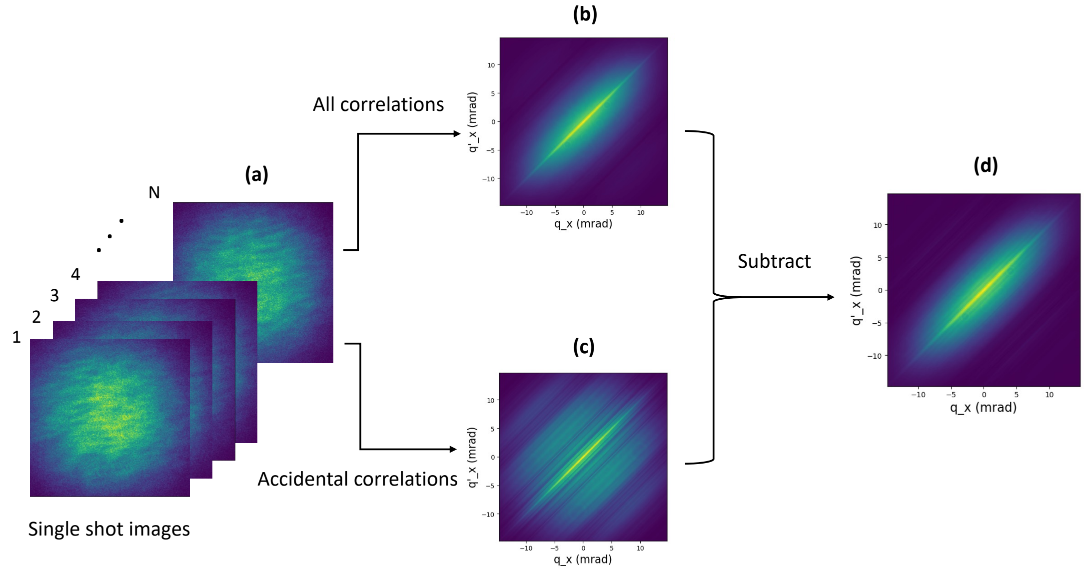

FIGURE 4.5: (a) Acquired single-shot images of the signal field's intensity pattern using EMCCD. N is the total number of images. (b) The total correlation. (c) The accidental correlation is the correlation between pixels from different images. (d) The real spatial first-order correlation function of the field is calculated by subtracting the accidental correlation from the total correlation.

accidental correlation (4.5(c)) using the second term in equation (4.5). To calculate the accidental correlation, we evaluate the correlation between each pair of consecutive images, denoted as $k' = k + 1$. Finally, the real first-order correlation function is obtained by subtracting the accidental correlation from the total correlation. Figure 4.6 illustrates the first-order correlation function for a single pump amplitude.

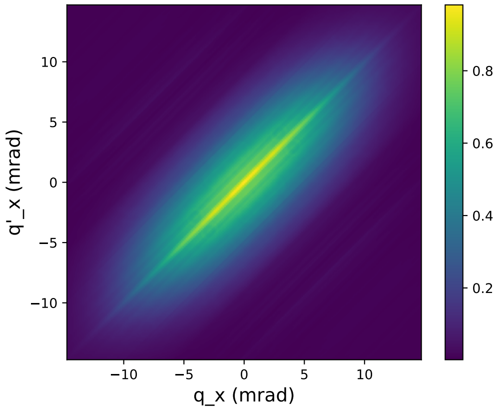

FIGURE 4.6: The first-order spatial correlation function $|G^{(1)}(q, q')|$ as a function of transverse wave vector coordinates $q_x$ and $q'_x$.

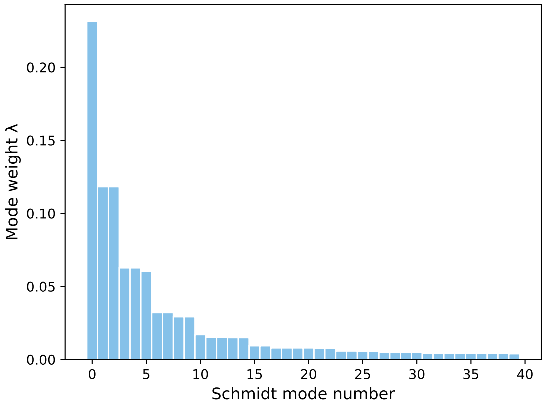

FIGURE 4.7: The experimentally reconstructed Schmidt spectrum for pump amplitude of $g = 1.66$ (arb units). The mode weights are normalized to their sum up to $40^{\text{th}}$ mode.

Now that we evaluated the first-order spatial correlation function from equation (4.5), as explained in section 3.2, we carry out coherent mode decomposition on it to obtain the Schmidt modes and Schmidt spectrum

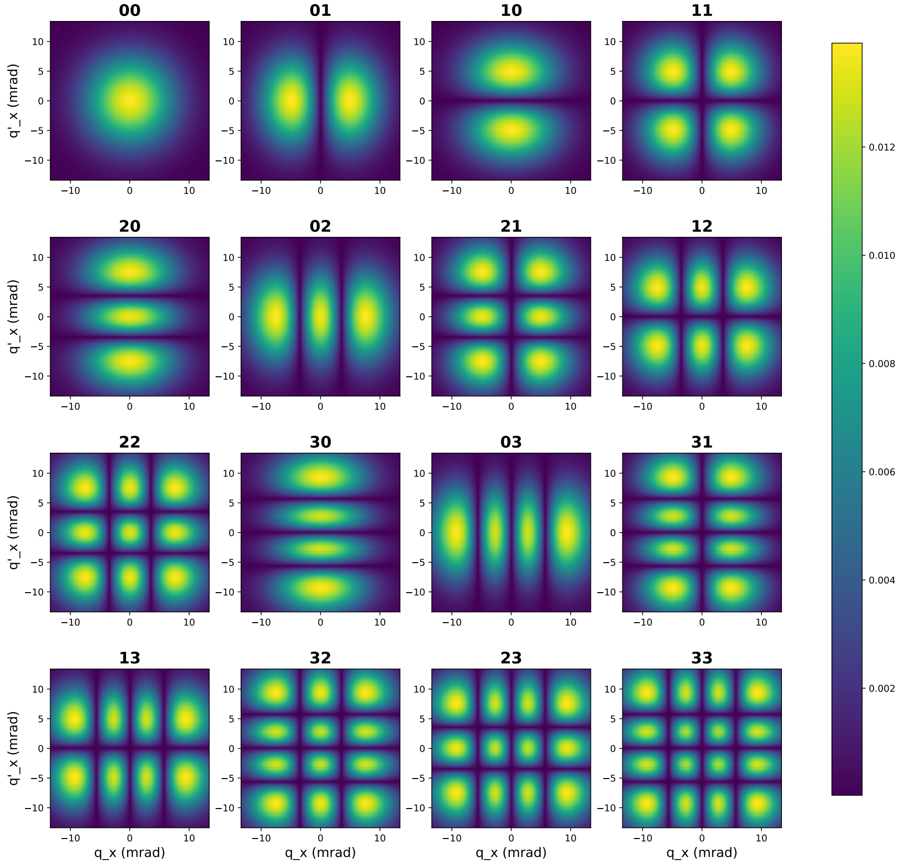

FIGURE 4.8: Experimentally constructed Schmidt modes for pump amplitude of $g = 1.66$ (arb units). The absolute values of the modes are plotted in this figure as a function of transverse wave vector coordinates $q_x$ and $q'_x$.

$$G^{(1)}(q, q') = \sum_j \lambda_j \nu_j^*(q) \nu_j(q'). \tag{4.6}$$

The Schmidt modes are obtained by finding the eigenvectors of the correlation matrix, and the eigenvalues construct the Schmidt spectrum. Our calculations assume rotational symmetry of the signal field, allowing us to compute the correlation function along the diametric slices of the intensity pattern. This results in a two-dimensional correlation function, $G^{(1)}(q, q')$, whose eigenvalues form the one-dimensional modes. To find two-dimensional Schmidt modes, we use an approach aligned with the method we proposed in Chapter 3, wherein we used rotational symmetry to construct the Schmidt spectrum and two-dimensional Schmidt modes by obtaining the tensor product of the one-dimensional eigenvalues and eigenvectors correspondingly

$$\lambda_{ij} = \lambda_i \otimes \lambda_j, \tag{4.7}$$

$$u_{ij} = \nu_i \otimes \nu_j. \tag{4.8}$$

In Figure 4.7 and Figure 4.8, we depict the Schmidt spectrum and absolute value of the first 16 Schmidt modes, respectively, for a single pump amplitude.

## 4.4 Evolution of the spatial correlations as a function of gain

In accordance with the procedure outlined in the previous section, we conducted the process for ten distinct pump amplitude values. We analyzed the changes in the Schmidt modes and Schmidt spectrum as the gain increased. As predicted based on the theoretical model presented in the previous chapter, we noted a progressive expansion of the spatial modes as the gain increases. This progression is visualized in Figure 4.9, which depicts the spatial modes for three different pump amplitude or gain values. In order to enhance our observation of the modes' growth, we visualized the one-dimensional cross-section of the mode 00 for three gain values, as depicted in figure 4.10. The FWHM of the first mode grows from 11.84 mrad to 12.09 mrad to 12.35 mrad when we increase the gain from $g = 1.47$ to $g = 1.56$ to $g = 1.66$ in arb units.

Furthermore, we find that the Schmidt spectrum becomes narrower with increasing gain. This result is in accordance with the predictions of the model stated in the previous chapter. Figure 4.11 presents the Schmidt spectrum for two gain values, demonstrating this behavior. In addition, figure 4.12 compares the theoretical and experimental Schmidt

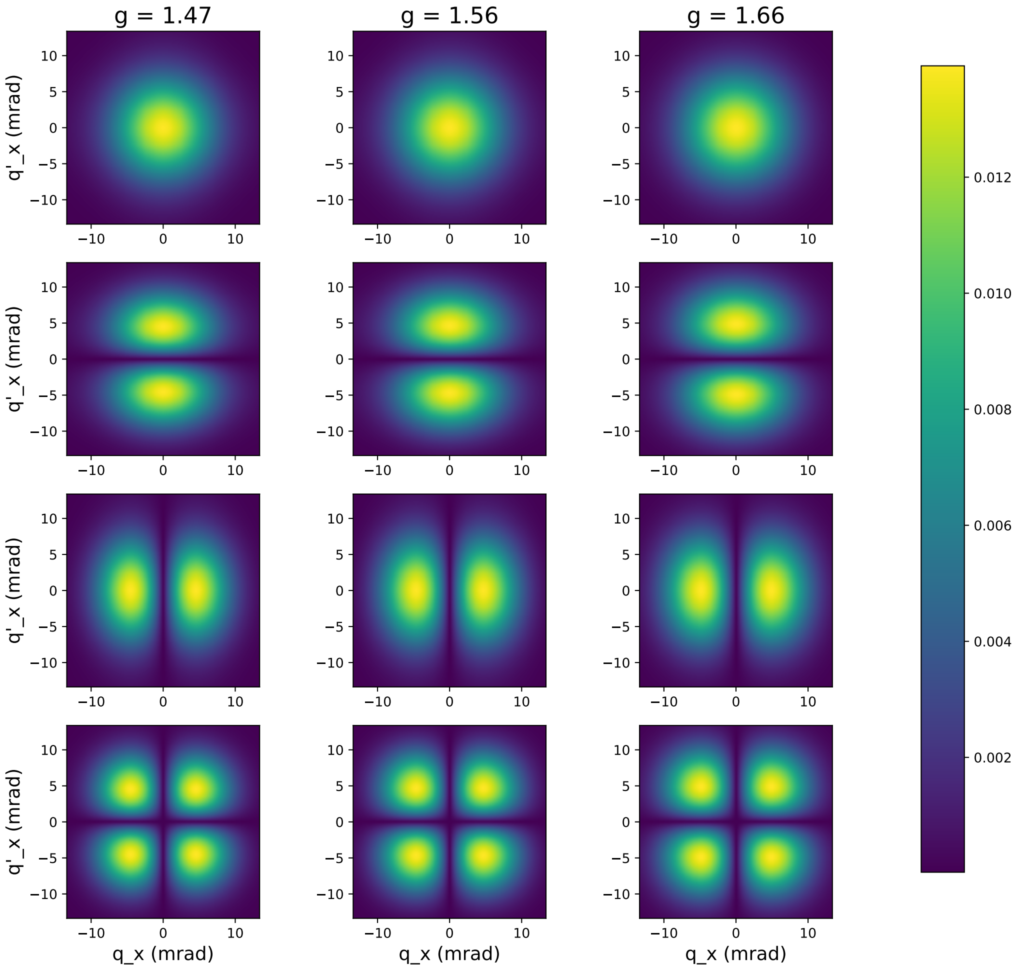

FIGURE 4.9: Experimentally constructed Schmidt modes for three different values of pump amplitude $g$. The spatial modes grow in size as the gain increases. The FWHM of the first mode grows from 11.84 mrad to 12.09 mrad to 12.35 mrad when we increase the gain from $g = 1.47$ to $g = 1.56$ to $g = 1.66$ in arb units.

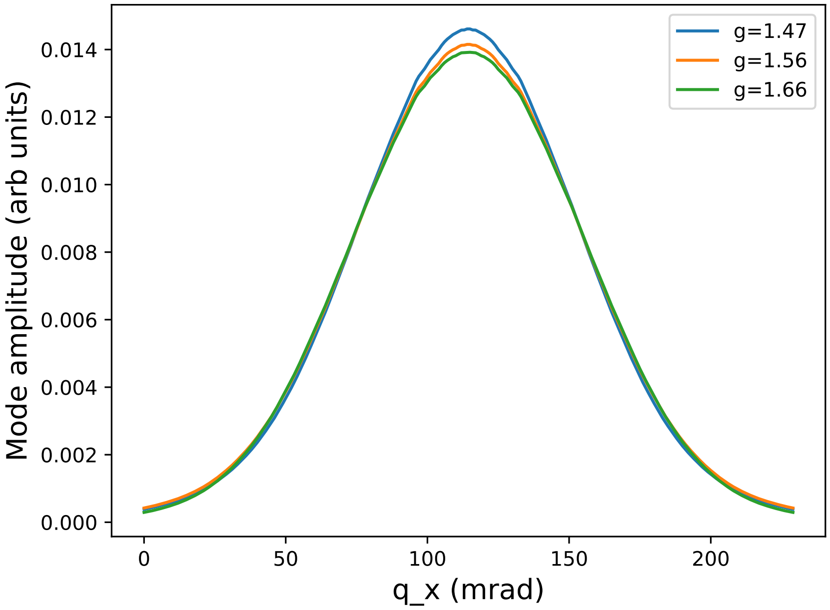

FIGURE 4.10: The cross sections of experimentally reconstructed two-dimensional Spatial Schmidt modes of high gain SPDC for two different gain values. The spatial modes grow in size as the gain increases. The FWHM of the first mode grows from 11.84 mrad to 12.09 mrad to 12.35 mrad when we increase the gain from $g = 1.47$ to $g = 1.56$ to $g = 1.66$ in arb units.

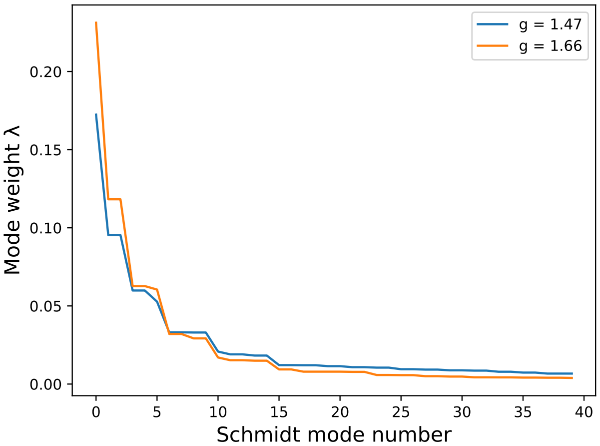

FIGURE 4.11: Schmidt spectrum for two different values of pump amplitude $g$. The spectrum narrows as the gain increases resulting in a fewer effective number of modes.

spectrum for two different values of gain.

As the gain increases, the spectrum narrows, and the Schmidt number decreases. This phenomenon has been predicted in the previous chapter, and Figure 4.13 provides quantitative evidence of this trend using both experimental results and theory. As shown in this figure, our experimental results are in good agreement with our theory, and they both show a decreasing trend in the Schmidt number as a function of the gain. In Chapter 2, we discussed that a higher Schmidt number signifies a greater level of entanglement between the two fields. Ultimately, our findings determine that the correlations between these entangled fields weaken as the gain increases. Additionally, the figure displays the total intensity of the generated field in relation to the pump amplitude.

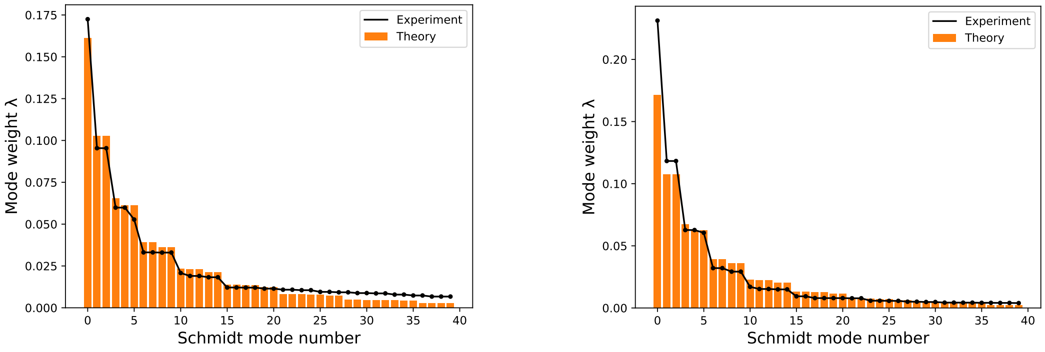

(a)

(b)

Figure 4.12: Schmidt spectrum constructed using theory (orange bars) and experiment (black dots) for gain values of (a) 1.47, and (b) 1.66 in arbitrary units.

Figure 4.13 demonstrates that the theory predicts a smaller change in the Schmidt number than the experiment. There are some possible explanations for this difference. Firstly, the numerical simulations assumed the signal, idler, and pump beams to be monochromatic. However, the experimental setup used a band-pass filter at the camera aperture to record the signal beam with a bandwidth of 10nm. The model can be improved by calculating the first-order correlation function for different wavelengths within the bandwidth of the signal field and taking a weighted average to determine $G^{(1)}(q, q')$. Secondly, the finite dimensions of the pixels may cause the experimentally measured $G^{(1)}(q, q')$ to be wider than the numerically constructed first-order correlation function, resulting in a discrepancy between the experimental and theoretical results.

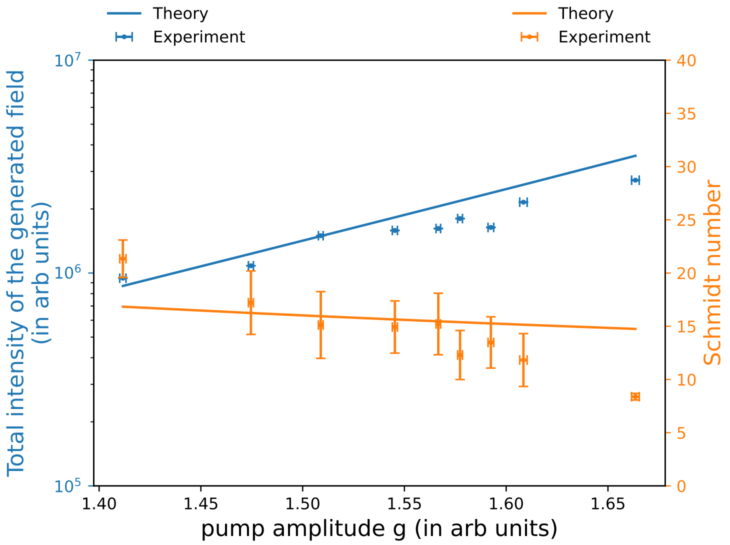

FIGURE 4.13: The Schmidt number and the total intensity as a function of pump amplitude $g$. There is a decreasing trend in the Schmidt modes as the gain increases in both experiment and theory. Also, the total intensity grows exponentially as a function of the gain.

## 4.5 Summary of the chapter

In this chapter, we experimentally test our model describing the spatial correlations of entangled light fields generated from high-gain SPDC. Our study characterized the evolution of the spatial correlations of the field generated through high-gain SPDC as a function of pump amplitude. Through experimental measurements, we determined their spatial correlations and gained valuable insights into their behavior under different conditions. Importantly, our experimental findings aligned with the predictions of our model for the spatial correlations of high-gain SPDC.

We presented an experimental method that allows us to determine two-dimensional profiles of the spatial Schmidt modes by directly measuring the intensity of the signal field and analyzing its spatial fluctuations. Unlike previous research, we assumed that the signal field is quasi-homogeneous and rotationally symmetric, which significantly sped up our computations.

Furthermore, we investigated the impact of the increasing gain on the spatial Schmidt modes and spectrum. Our experimental results confirmed the theoretical findings discussed in the previous chapter. As the gain increased, we observed a growth in the size of the spatial Schmidt modes and a narrowing trend in the Schmidt spectrum. Additionally, we noted a decrease in the Schmidt number as the gain increased. In the upcoming chapter, we summarize our results and suggest some prospects for future work.

## Chapter 5

# Summary and outlook

In this thesis, we theoretically model and experimentally characterize the spatial correlations of entangled light fields generated in high-gain spontaneous parametric down-conversion (SPDC). The phenomenon of SPDC involves the interaction between a nonlinear medium and a strong pump field, leading to the generation of two entangled fields referred to as the signal and idler. We apply the Schmidt decomposition technique to quantify the spatial correlations between these fields. Furthermore, we perform a coherent mode decomposition on the first-order coherence function of the signal field to determine the entangled fields' Schmidt modes and spectrum. Moreover, we measure the degree of entanglement between the two fields by calculating the Schmidt number, which reflects the effective number of non-zero terms in the Schmidt decomposition.

The first-order correlation function is often measured through interferometry. However, in the case of thermal fields, the first and second-order correlation functions are related, thereby enabling the first-order correlation function to be derived from the second-order correlation function. As the joint state describing the signal and idler fields is a bipartite squeezed state, the individual signal and idler fields exhibit thermal statistics. As a result, it is possible to determine the first-order coherence function indirectly by first measuring the second-order coherence function from the statistics of intensity fluctuations and then using the Siegert relation to determine the first-order coherence function. This is an easier task than measuring the first-order correlation function directly using interferometry. We then construct the Schmidt modes and Schmidt spectrum from the eigenvectors and eigenvalues of the first-order correlation function, respectively. The existing procedures for computing the Schmidt modes and Schmidt spectrum were computationally intensive, including performing eigendecomposition on a four-dimensional correlation function. In contrast with previous studies, we exploit the symmetries of the correlations and vastly reduce the computation time. We perform our analysis for different values of the pump amplitude or, equivalently, the gain. Our findings theoretically and experimentally describe the change in spatial correlations as a function of the pump amplitude (gain).

In Chapter 1, we presented a survey of previous studies on quantum entanglement and spontaneous parametric down-conversion. In Chapter 2, we introduced the key concepts used in this study. In Chapter 3, we introduced the theoretical framework employed to illustrate the development of Schmidt modes and Schmidt spectrum with increasing gain. We obtained the Schmidt modes and spectrum by performing an eigendecomposition on the measured first-order correlation function based on the theoretical model we presented. Our method differs from previous techniques in the literature as we exploit the assumptions of isotropy and quasi-homogeneity of the first-order correlation function to enhance the computational efficiency of our analysis. Our theoretical study predicts an enlargement in the size of the spatial Schmidt modes, demonstrated by an increase in the full width at half maximum (FWHM) of the spatial modes as the gain increases. In addition, our model suggests that the Schmidt spectrum narrows as the gain increases. As the Schmidt spectrum narrows with increasing gain, the Schmidt number also decreases. This decrease in the Schmidt number at higher gains demonstrates that the entanglement between the signal and idler fields weakens with increasing gain.

In Chapter 4 of this thesis, we test our model's predictions through experimental characterization of the spatial correlations. To achieve this, we analyze the statistics of the signal field's intensity fluctuations to find the second-order correlation function, and from there, we determine the first-order coherence function by utilizing the thermal nature of the signal field. Additionally, to reduce computation time, we assume that the signal field is rotationally symmetric while analyzing the experimental data. We find that our experimental observations are in good agreement with our model's predictions. Our experimental results reveal that the FWHM of the first Schmidt mode changes from 11.84 mrad to 12.35 mrad when the pump amplitude changes by a factor of 1.42. Furthermore, in accordance with our model's predictions, the Schmidt spectrum narrows as the gain increases, causing the Schmidt number to decrease from 8.38 to 17.21 when the pump amplitude changes by a factor of 1.42.

Our work on characterizing the Schmidt mode and Schmidt spectrum of high-gain SPDC paves the way for future research. In this thesis, we primarily investigate the collinear type of SPDC. Nevertheless, one can conduct experiments using the crystal angle set to generate non-collinear SPDC. Our method can be used to explore if the spatial high-gain SPDC correlations exhibit the same trend with increasing gain in the non-collinear emission as in the collinear one.

Furthermore, in the research presented in this thesis, we quantify the correlations of high-gain SPDC for a pump with a Gaussian profile. As a follow-up research, one can investigate the spatial correlations of high-gain SPDC using a structured pump. However, it is important to note that the assumptions employed in the analysis of this thesis to improve the calculation's efficiency are only applicable if the generated SPDC field is rotationally symmetric.

Our research holds significant potential implications for quantum imaging, particularly in exploring new avenues for advancing the field. Previous studies on quantum imaging have primarily focused on the low-gain regime, where the signal-to-noise ratio is relatively low compared to the high-gain regime. The correlation between signal and idler fields was exploited to subtract the noise and produce clear images effectively [97]. Conversely, the high-gain regime offers a substantially higher classical signal-to-noise ratio. However, our work shows that the correlation between the entangled fields decreases as the gain increases. Through our investigation into the evolution of spatial correlations with gain, our work presents a valuable pathway toward optimizing quantum imaging techniques and deepening our understanding of this fascinating domain.

# Bibliography

[1] A. A. Michelson. I. on the application of interference methods to astronomical measurements. *The London, Edinburgh, and Dublin Philosophical Magazine and Journal of Science*, 30(182):1–21, 1890.

[2] A. A. Michelson. Measurement of jupiter's satellites by interference. *Nature*, 45, 1891.

[3] A. A. Michelson. Xxx. on the application of interference methods to spectroscopic measurements.,Äîii. *The London, Edinburgh, and Dublin Philosophical Magazine and Journal of Science*, 34(208):280–299, 1892.

[4] F. Zernike. The concept of degree of coherence and its application to optical problems. *Physica*, 5(8):785–795, 1938.

[5] R. H. Brown and R. Q. Twiss. Correlation between photons in two coherent beams of light. *Nature*, 177, 1956.

[6] R. H. Brown and R. Q. Twiss. Interferometry of the intensity fluctuations in light. i. basic theory: The correlation between photons in coherent beams of radiation. *Proceedings of the Royal Society of London. Series A, Mathematical and Physical Sciences*, 242, 1957.

[7] L. Mandel and E. Wolf. Coherence properties of optical fields. *Rev. Mod. Phys.*, 37:231–287, Apr 1965.

[8] M. Born, E. Wolf, A. B. Bhatia, P. C. Clemmow, D. Gabor, A. R. Stokes, A. M. Taylor, P. A. Wayman, and W. L. Wilcock. *Principles of Optics: Electromagnetic Theory of Propagation, Interference and Diffraction of Light.* Cambridge University Press, 7 edition, 1999.

[9] R. J. Glauber. The quantum theory of optical coherence. *Phys. Rev.*, 130:2529–2539, Jun 1963.

[10] R. J. Glauber. Coherent and incoherent states of the radiation field. *Phys. Rev.*, 131:2766–2788, Sep 1963.

[11] A. Einstein, B. Podolsky, and N. Rosen. Can quantum-mechanical description of physical reality be considered complete? *Phys. Rev.*, 47:777–780, May 1935.

[12] N. Bohr. Can quantum-mechanical description of physical reality be considered complete? *Phys. Rev.*, 48:696–702, Oct 1935.

[13] E. Schrödinger. Die gegenwärtige situation in der quantenmechanik. *Naturwissenschaften*, 23:807–812, 1935.

[14] J. S. Bell. On the einstein podolsky rosen paradox. *Physics Physique Fizika*, 1:195–200, Nov 1964.

[15] A. Aspect, P. Grangier, and G. Roger. Experimental tests of realistic local theories via bell's theorem. *Phys. Rev. Lett.*, 47:460–463, Aug 1981.

[16] A. Aspect, P. Grangier, and G. Roger. Experimental realization of einstein-podolsky-rosen-bohm gedankenexperiment: A new violation of bell's inequalities. *Phys. Rev. Lett.*, 49:91–94, Jul 1982.

[17] S. J. Freedman and J. F. Clauser. Experimental test of local hidden-variable theories. *Phys. Rev. Lett.*, 28:938–941, Apr 1972.

[18] Z. Y. Ou and L. Mandel. Violation of bell's inequality and classical probability in a two-photon correlation experiment. *Phys. Rev. Lett.*, 61:50–53, Jul 1988.

[19] G. Weihs, T. Jennewein, C. Simon, H. Weinfurter, and A. Zeilinger. Violation of bell's inequality under strict einstein locality conditions. *Phys. Rev. Lett.*, 81:5039–5043, Dec 1998.

[20] L. K. Shalm, E. Meyer-Scott, B. G. Christensen, P. Bierhorst, M. A. Wayne, M. J. Stevens, T. Gerrits, S. Glancy, D. R. Hamel, M. S. Allman, K. J. Coakley, S. D. Dyer, C. Hodge, A. E. Lita, V. B. Verma, C. Lambrocco, E. Tortorici, A. L. Migdall, Y. Zhang, D. R. Kumor, W. H. Farr, F. Marsili, M. D. Shaw, J. A. Stern, C. Abellán, W. Amaya, V. Pruneri, T. Jennewein, M. W. Mitchell, P. G. Kwiat, J. C. Bienfang, R. P. Mirin, E. Knill, and S. Nam. Strong loophole-free test of local realism. *Phys. Rev. Lett.*, 115:250402, Dec 2015.

[21] A. E. Dréau A. Reiserer N. Kalb M. S. Blok J. Ruitenberg R. F. L. Vermeulen R. N. Schouten C. Abellán W. Amaya V. Pruneri M. W. Mitchell M. Markham D. J. Twitchen D. Elkouss S. Wehner T. H. Taminiau R. Hanson B. Hensen, H. Bernien. Loophole-free bell inequality violation using electron spins separated by 1.3 kilometres. *Nature*, 2015.

[22] C. H. Bennett, G. Brassard, C. Crépeau, R. Jozsa, A. Peres, and W. K. Wootters. Teleporting an unknown quantum state via dual classical and einstein-podolsky-rosen channels. *Phys. Rev. Lett.*, 70:1895–1899, Mar 1993.

[23] C. H. Bennett and S. J. Wiesner. Communication via one- and two-particle operators on einstein-podolsky-rosen states. *Phys. Rev. Lett.*, 69:2881–2884, Nov 1992.

[24] P.W. Shor. Algorithms for quantum computation: discrete logarithms and factoring. In *Proceedings 35th Annual Symposium on Foundations of Computer Science*, pages 124–134, 1994.

[25] M. A. Nielsen and I. L. Chuang. *Quantum Computation and Quantum Information: 10th Anniversary Edition.* Cambridge University Press, 2010.

[26] R. Horodecki, P. Horodecki, M. Horodecki, and K. Horodecki. Quantum entanglement. *Rev. Mod. Phys.*, 81:865–942, Jun 2009.

[27] R. W. Boyd. *Nonlinear Optics.* 2008.

[28] Klyshko D.N. Zel'dovich B.Ya. Field statistics in parametric luminescence. *JETP Lett.*, 9:69.

[29] D. C. Burnham and D. L. Weinberg. Observation of simultaneity in parametric production of optical photon pairs. *Phys. Rev. Lett.*, 25:84–87, Jul 1970.

[30] C. H. Bennett, F. Bessette, G. Brassard, L. Salvail, and J. A. Smolin. Experimental quantum cryptography. *J. Cryptology*, 5:3–28, 1992.

[31] S. Grblacher, T. Jennewein, A. Vaziri, G. Weihs, and A. Zeilinger. Experimental quantum cryptography with qutrits. *New Journal of Physics*, 8(5):75, may 2006.

[32] Drmota P. Nichol B.C. et al. Nadlinger, D. P. Experimental quantum key distribution certified by bell's theorem. *Nature*, 2022.

[33] V. Giovannetti, S. Lloyd, and L. Maccone. Quantum-enhanced measurements: Beating the standard quantum limit. *Science*, 306(5700):1330–1336, 2004.

[34] T. Nagata, R. Okamoto, J. L. O'Brien, K. Sasaki, and S. Takeuchi. Beating the standard quantum limit with four-entangled photons. *Science*, 316(5825):726–729, 2007.

[35] C. K. Hong and L. Mandel. Experimental realization of a localized one-photon state. *Phys. Rev. Lett.*, 56:58–60, Jan 1986.

[36] C. H. Bennett, D. P. DiVincenzo, J. A. Smolin, and W. K. Wootters. Mixed-state entanglement and quantum error correction. *Phys. Rev. A*, 54:3824–3851, Nov 1996.

[37] W. K. Wootters. Entanglement of formation of an arbitrary state of two qubits. *Phys. Rev. Lett.*, 80:2245–2248, Mar 1998.

[38] R. Horodecki, P. Horodecki, M. Horodecki, and K. Horodecki. Quantum entanglement. *Rev. Mod. Phys.*, 81:865–942, Jun 2009.

[39] A. Joobeur, B. E. A. Saleh, and M. C. Teich. Spatiotemporal coherence properties of entangled light beams generated by parametric down-conversion. *Phys. Rev. A*, 50:3349–3361, Oct 1994.

[40] P. H. S. Ribeiro, S. Pádua, J. C. Machado da Silva, and G. A. Barbosa. Controlling the degree of visibility of young's fringes with photon coincidence measurements. *Phys. Rev. A*, 49:4176–4179, May 1994.

[41] C. H. Monken, P. H. Souto Ribeiro, and S. Pádua. Transfer of angular spectrum and image formation in spontaneous parametric down-conversion. *Phys. Rev. A*, 57:3123–3126, Apr 1998.

[42] E. J. S. Fonseca, C. H. Monken, and S. Pádua. Measurement of the de broglie wavelength of a multiphoton wave packet. *Phys. Rev. Lett.*, 82:2868–2871, Apr 1999.

[43] Markus Hiekkamäki, Rafael Barros, Marco Ornigotti, and Robert Fickler. Observation of the quantum gouy phase. *Nature Photonics*, 16:1–6, 10 2022.

[44] W. A. T. Nogueira, S. P. Walborn, S. Pádua, and C. H. Monken. Experimental observation of spatial antibunching of photons. *Phys. Rev. Lett.*, 86:4009–4012, Apr 2001.

[45] W. A. T. Nogueira, S. P. Walborn, S. Pádua, and C. H. Monken. Spatial antibunching of photons with parametric down-conversion. *Phys. Rev. A*, 66:053810, Nov 2002.

[46] J. C. Howell, R. S. Bennink, S. J. Bentley, and R. W. Boyd. Realization of the einstein-podolsky-rosen paradox using momentum- and position-entangled photons from spontaneous parametric down conversion. *Phys. Rev. Lett.*, 92:210403, May 2004.

[47] M. D'Angelo, Y. Kim, S. P. Kulik, and Y. Shih. Identifying entanglement using quantum ghost interference and imaging. *Phys. Rev. Lett.*, 92:233601, Jun 2004.

[48] F. M. Miatto, H. Di Lorenzo Pires, S. M. Barnett, and M. P. van Exter. Spatial Schmidt modes generated in parametric down-conversion. *European Physical Journal D*, 66(10):263, October 2012.

[49] S. S. Straupe, D. P. Ivanov, A. A. Kalinkin, I. B. Bobrov, and S. P. Kulik. Angular schmidt modes in spontaneous parametric down-conversion. *Phys. Rev. A*, 83:060302, Jun 2011.

[50] M. P. van Exter, A. Aiello, S. S. R. Oemrawsingh, G. Nienhuis, and J. P. Woerdman. Effect of spatial filtering on the schmidt decomposition of entangled photons. *Phys. Rev. A*, 74:012309, Jul 2006.

[51] F. Miatto, T. Brougham, and A. Yao. Cartesian and polar schmidt bases for down-converted photons. *The European Physical Journal D*, 66, 11 2011.

[52] C. K. Hong and L. Mandel. Theory of parametric frequency down conversion of light. *Phys. Rev. A*, 31:2409–2418, Apr 1985.

[53] T. E. Keller and M. H. Rubin. Theory of two-photon entanglement for spontaneous parametric down-conversion driven by a narrow pump pulse. *Phys. Rev. A*, 56:1534–1541, Aug 1997.

[54] W. P. Grice and I. A. Walmsley. Spectral information and distinguishability in type-ii down-conversion with a broadband pump. *Phys. Rev. A*, 56:1627–1634, Aug 1997.

[55] A. I. Lvovsky. *Squeezed Light*, chapter 5, pages 121–163. John Wiley Sons, Ltd, 2015.

[56] J. Aasi, J. Abadie, and B. et al. Abbott. Enhanced sensitivity of the ligo gravitational wave detector by using squeezed states of light. *Nature Photonics*, 7:613, 07 2013.

[57] C. K. Law and J. H. Eberly. Analysis and interpretation of high transverse entanglement in optical parametric down conversion. *Phys. Rev. Lett.*, 92:127903, Mar 2004.

[58] P. Sharapova, A. M. Pérez, O. V. Tikhonova, and M. V. Chekhova. Schmidt modes in the angular spectrum of bright squeezed vacuum. *Phys. Rev. A*, 91:043816, Apr 2015.

[59] V. A. Averchenko, G. Frascella, M. Kalash, A. Cavanna, and M. V. Chekhova. Reconstructing two-dimensional spatial modes for classical and quantum light. *Phys. Rev. A*, 102:053725, Nov 2020.

[60] F. L. Pedrotti, L. M. Pedrotti, and L. S. Pedrotti. *Introduction to Optics*. Cambridge University Press, 3 edition, 2017.

[61] A. A. Michelson and E. W. Morley. On the relative motion of the earth and the luminiferous ether. *American Journal of Science*, s3-34(203):333–345, 1887.

[62] M. Lahiri. *Coherence and Statistical Optics*, chapter 2, pages 27–60. John Wiley Sons, Ltd, 2015.

[63] L. Mandel and E. Wolf. *Optical Coherence and Quantum Optics*. Cambridge University Press, 1995.

[64] M. Chekhova and S. Kulik. *Physical Foundations of Quantum Electronics by David Klyshko*. WORLD SCIENTIFIC, 2011.

[65] V. Lakshminarayanan, M. Calvo, and T. Alieyva. *Mathematical Optics Classical,Quantum and Computational Methods*. 12 2012.

[66] A.S. Ostrovsky. *Coherent-mode Representations in Optics*. Press Monographs. Society of Photo Optical, 2006.

[67] E. Wolf. New theory of partial coherence in the space–frequency domain. part i: spectra and cross spectra of steady-state sources. *J. Opt. Soc. Am.*, 72(3):343–351, Mar 1982.

[68] R. Martínez-Herrero. Expansion of complex degree of coherence. *Il Nuovo Cimento B (1971-1996)*, 54:205–210, 11 1979.

[69] A. M. Wazwaz. *Linear and Nonlinear Integral Equations; Methods and Applications*. Springer Berlin, Heidelberg, 2011.

[70] Ö. Bjrck. Numerics of gram-schmidt orthogonalization. *Linear Algebra and its Applications*, 197-198:297–316, 1994.

[71] R. H. Brown and R.Q. Twiss. Lxxiv. a new type of interferometer for use in radio astronomy. *The London, Edinburgh, and Dublin Philosophical Magazine and Journal of Science*, 45(366):663–682, 1954.

[72] Y. Shih. *An Introduction to Quantum Optics: Photon and Biphoton Physics*. Series in Optics and Optoelectronics Series. CRC Press, Taylor & Francis Group, 2020.

[73] A.J.F. Siegert. *On the Fluctuations in Signals Returned by Many Independently Moving Scatterers*. Report (Massachusetts Institute of Technology. Radiation Laboratory). Radiation Laboratory, Massachusetts Institute of Technology, 1943.

[74] R. Loudon. *The Quantum Theory of Light*. Oxford science publications. Oxford University Press, 2003.

[75] D. Walls and G. Milburn. *Quantum Optics*. 2008.

[76] P. et al. Lassègues. Field and intensity correlations: the Siegert relation from stars to quantum emitters. *Eur. Phys. J. D*, 76(12):246, 2022.

[77] D. Ferreira, R. Bachelard, W. Guerin, R. Kaiser, and M. Fouch©. Connecting field and intensity correlations: The Siegert relation and how to test it. *American Journal of Physics*, 88(10):831–837, 10 2020.

[78] C. Roychoudhuri, A.F. Kracklauer, and K. Creath. *The Nature of Light: What is a Photon?* 2008.

[79] A. Muthukrishnan, M.O. Scully, and M. Zubairy. The concept of the photon - revisited. *Optics and Photonics News*, 14:18–27, 10 2003.

[80] M. O. Scully and M. S. Zubairy. *Quantum Optics*. Cambridge University Press, 1997.

[81] G. Benenti, G. Casati, and G. Strini. *Principles of Quantum Computation and Information: Volume II: Basic Tools and Special Topics*. 03 2007.

[82] Daniel A. S. *Quantum and Atom Optics*. 2023.

[83] O. Gºhne and G. Tth. Entanglement detection. *Physics Reports*, 474(1):1–75, 2009.

[84] J. Preskill. *Lecture Notes for Physics 229: Quantum Information and Computation*. 1998.

[85] D. Bruss and G. Leuchs. Lectures on quantum information. 02 2008.

[86] G. Kulkarni. *Novel tools for characterizing photon correlations in parametric down-conversion*. 2019.

[87] A. Peres. *Quantum Theory: Concepts and Methods*. 2002.

[88] A. K. Ekert and P. L. Knight. Entangled quantum systems and the schmidt decomposition. *American Journal of Physics*, 63:415–423, 1995.

[89] H. D. Saleh, S. Vezzoli, L. Caspani, A. Branny, S. Kumar, B. Gerardot, and D. Faccio. Towards spontaneous parametric down conversion from monolayer mos2. *Scientific Reports*, 8, 03 2018.

[90] G. Kulkarni, J. Rioux, B. Braverman, M. V. Chekhova, and R. W. Boyd. Classical model of spontaneous parametric down-conversion. *Phys. Rev. Res.*, 4:033098, Aug 2022.

[91] Y. H. Shih and C. O. Alley. New type of einstein-podolsky-rosen-bohm experiment using pairs of light quanta produced by optical parametric down conversion. *Phys. Rev. Lett.*, 61:2921–2924, Dec 1988.

[92] X. Y. Zou, L. J. Wang, and L. Mandel. Induced coherence and indistinguishability in optical interference. *Phys. Rev. Lett.*, 67:318–321, Jul 1991.

[93] C. K. Hong, Z. Y. Ou, and L. Mandel. Measurement of subpicosecond time intervals between two photons by interference. *Phys. Rev. Lett.*, 59:2044–2046, Nov 1987.

[94] N. Gisin, G. Ribordy, W. Tittel, and H. Zbinden. Quantum cryptography. *Rev. Mod. Phys.*, 74:145–195, Mar 2002.

[95] P. Moreau, E. Toninelli, T. Gregory, and M. Padgett. Imaging with quantum states of light. *Nature Reviews Physics*, 1:1, 05 2019.

[96] O. Jedrkiewicz, Y. K. Jiang, E. Brambilla, A. Gatti, M. Bache, L. A. Lugiato, and P. Di Trapani. Detection of sub-shot-noise spatial correlation in high-gain parametric down conversion. *Phys. Rev. Lett.*, 93:243601, Dec 2004.

[97] G. Brida, M. Genovese, and I. Ruo Berchera. Experimental realization of sub-shot-noise quantum imaging. *Nature Photonics*, 4(4):227–230, April 2010.

[98] L. Mandel. Photon interference and correlation effects produced by independent quantum sources. *Phys. Rev. A*, 28:929–943, Aug 1983.

[99] R. Ghosh, C. K. Hong, Z. Y. Ou, and L. Mandel. Interference of two photons in parametric down conversion. *Phys. Rev. A*, 34:3962–3968, Nov 1986.

[100] C. K. Hong and T. G. Noh. Two-photon double-slit interference experiment. *J. Opt. Soc. Am. B*, 15(3):1192–1197, Mar 1998.

[101] D. V. Strekalov, A. V. Sergienko, D. N. Klyshko, and Y. H. Shih. Observation of two-photon “ghost” interference and diffraction. *Phys. Rev. Lett.*, 74:3600–3603, May 1995.

[102] F. Miatto, H. Pires, S. Barnett, and M. Exter. Spatial schmidt modes generated in parametric downconversion. *The European Physical Journal D*, 66, 01 2012.

[103] P. Sharapova, A. M. Pérez, O. V. Tikhonova, and M. V. Chekhova. Schmidt modes in the angular spectrum of bright squeezed vacuum. *Phys. Rev. A*, 91:043816, Apr 2015.

[104] M. H. Rubin. Transverse correlation in optical spontaneous parametric down-conversion. *Phys. Rev. A*, 54:5349–5360, Dec 1996.

[105] A. Jha and R. W. Boyd. Spatial two-photon coherence of the entangled field produced by down-conversion using a partially spatially coherent pump beam. *Phys. Rev. A*, 81:013828, Jan 2010.

[106] C. K. Hong and L. Mandel. Theory of parametric frequency down conversion of light. *Phys. Rev. A*, 31:2409–2418, Apr 1985.

[107] N. Quesada and J. E. Sipe. Effects of time ordering in quantum nonlinear optics. *Phys. Rev. A*, 90:063840, Dec 2014.

[108] A. M. BraÑczyk, T. M. Stace, and T. C. Ralph. Time Ordering in Spontaneous Parametric Down‚Äêconversion. *AIP Conference Proceedings*, 1363(1):335–338, 10 2011.

[109] A. Christ, K. Laiho, A. Eckstein, K. N. Cassemiro, and C. Silberhorn. Probing multimode squeezing with correlation functions. *New Journal of Physics*, 13(3):033027, mar 2011.

[110] P. Sharapova, A. M. Pérez, O. V. Tikhonova, and M. V. Chekhova. Schmidt modes in the angular spectrum of bright squeezed vacuum. *Phys. Rev. A*, 91:043816, Apr 2015.

[111] K. Yu. Spasibko, T. Sh. Iskhakov, and M. V. Chekhova. Spectral properties of high-gain parametric down-conversion. *Opt. Express*, 20(7):7507–7515, Mar 2012.

[112] P. R. Sharapova, G. Frascella, M. Riabinin, A. M. Pérez, O. V. Tikhonova, S. Lemieux, R. W. Boyd, G. Leuchs, and M. V. Chekhova. Properties of bright squeezed vacuum at increasing brightness. *Phys. Rev. Res.*, 2:013371, Mar 2020.

[113] L. A. Lugiato, A. Gatti, and E. Brambilla. Quantum imaging. *Journal of Optics B: Quantum and Semiclassical Optics*, 4(3):S176, mar 2002.

[114] V. Boyer, A. M. Marino, R. C. Pooser, and P. D. Lett. Entangled images from four-wave mixing. *Science*, 321(5888):544–547, 2008.

[115] M. Chekhova and Z. Ou. Nonlinear interferometers in quantum optics. *Advances in Optics and Photonics*, 8:104, 03 2016.

[116] S. Lemieux, M. Manceau, P. R. Sharapova, O. V. Tikhonova, R. W. Boyd, G. Leuchs, and M. V. Chekhova. Engineering the frequency spectrum of bright squeezed vacuum via group velocity dispersion in an su(1,1) interferometer. *Phys. Rev. Lett.*, 117:183601, Oct 2016.

[117] A. Einstein. Über einen die Erzeugung und Verwandlung des Lichtes betreffenden heuristischen Gesichtspunkt. *Annalen der Physik*, 322(6):132–148, January 1905.

[118] P. Dirac and N. Bohr. The quantum theory of the emission and absorption of radiation. *Proceedings of the Royal Society of London. Series A, Containing Papers of a Mathematical and Physical Character*, 114(767):243–265, 1927.

[119] C. Gerry and P. Knight. *Introductory Quantum Optics*. Cambridge University Press, 2004.

[120] D. J. Griffiths and D. F. Schroeter. *Introduction to Quantum Mechanics*. Cambridge University Press, 3 edition, 2018.

[121] D.L. Andrews. *Photonics, Volume 1: Fundamentals of Photonics and Physics.* A Wiley-Science Wise Co-Publication. Wiley, 2015.

[122] A. Christ, K. Laiho, A. Eckstein, K. Cassemiro, and C. Silberhorn. Probing multimode squeezing with correlation functions. *New Journal of Physics - NEW J PHYS*, 13, 03 2011.

[123] S. Barnett and P.M. Radmore. *Methods in Theoretical Quantum Optics.* Oxford Series in Optical and Imaging Sciences. Clarendon Press, 2002.

[124] B. Stiller, U. Seyfarth, and G. Leuchs. Temporal and spectral properties of quantum light. 11 2014.

[125] D. B. Horoshko, S. De Bièvre, G. Patera, and M. I. Kolobov. Thermal-difference states of light: Quantum states of heralded photons. *Phys. Rev. A*, 100:053831, Nov 2019.

[126] B. Yurke and M. Potasek. Obtainment of thermal noise from a pure quantum state. *Phys. Rev. A*, 36:3464–3466, Oct 1987.

[127] M. Avenhaus, H. B. Coldenstrodt-Ronge, K. Laiho, W. Mauerer, I. A. Walmsley, and C. Silberhorn. Photon number statistics of multimode parametric down-conversion. *Phys. Rev. Lett.*, 101:053601, Aug 2008.

[128] A. Eckstein, A. Christ, P. J. Mosley, and C. Silberhorn. A bright, pulsed two-mode squeezer. *arXiv e-prints*, page arXiv:1006.5667, June 2010.

[129] M. Naraschewski and R. J. Glauber. Spatial coherence and density correlations of trapped bose gases. *Phys. Rev. A*, 59:4595–4607, Jun 1999.

[130] H. Di Lorenzo Pires, C. H. Monken, and M. P. van Exter. Direct measurement of transverse-mode entanglement in two-photon states. *Phys. Rev. A*, 80:022307, Aug 2009.

[131] A. K. Jha. *Coherence Properties of the Entangled Two-Photon Field Produced by Parametric Down-Conversion.* 2009.

[132] D. N. Klyshko. *Photons Nonlinear Optics.* CRC Press, 2018.

[133] E. Brambilla, A. Gatti, M. Bache, and L. A. Lugiato. Simultaneous near-field and far-field spatial quantum correlations in the high-gain regime of parametric down-conversion. *Phys. Rev. A*, 69:023802, Feb 2004.

[134] D. Eimerl, L. Davis, S. Velsko, E. K. Graham, and A. Zalkin. Optical, mechanical, and thermal properties of barium borate. *Journal of Applied Physics*, 62(5):1968–1983, 09 1987.

[135] H. Di Lorenzo Pires and M. P. van Exter. Observation of near-field correlations in spontaneous parametric down-conversion. *Phys. Rev. A*, 79:041801, Apr 2009.

[136] A. Bhattacharjee, M. Joshi, S. Karan, J. Leach, and A. Jha. Propagation-induced revival of entanglement in the angle-oam bases. *Science Advances*, 8, 08 2022.

[137] H. Defienne, M. Reichert, and J. W. Fleischer. General model of photon-pair detection with an image sensor. *Phys. Rev. Lett.*, 120:203604, May 2018.

[138] H. Defienne M. Reichert and J. W. Fleischer. Massively parallel coincidence counting of high-dimensional entangled states. *Scientific Reports*, 8:203604, May 2018.